1-2016

# Conterminous United States Crop Field Size Quantification from Multi-temporal Landsat Data

Lin Yan Dr.
*South Dakota State University*, lin.yan@sdstate.edu

David P. Roy
*South Dakota State University*, david.roy@sdstate.edu

CrossMark

# Conterminous United States crop field size quantification from multi-temporal Landsat data

L. Yan \*, D.P. Roy

*Geospatial Sciences Center of Excellence, South Dakota State University, Brookings, SD 57007, USA*

## ABSTRACT

Agricultural field size is indicative of the degree of agricultural capital investment, mechanization and labor intensity, and it is ecologically important. A recently published automated computational methodology to extract agricultural crop fields from weekly 30 m Web Enabled Landsat data (WELD) time series was refined and applied to a year of Landsat 5 Thematic Mapper (TM) and Landsat 7 Enhance Thematic Mapper Plus (ETM +) acquisitions for all of the conterminous United States (CONUS). For the first time, spatially explicit CONUS field size maps and derived information are presented. A total of 4,182,777 fields were extracted with mean and median field sizes of 0.193 km$^2$ and 0.278 km$^2$, respectively. The CONUS field size histogram was skewed; 50% of the extracted fields had sizes greater than or smaller than 0.361 km$^2$, and there were four distinct peaks that corresponded closely to sizes equivalent to fields with 0.25 × 0.25 mile, 0.25 × 0.5 mile, 0.5 × 0.5 mile, and 0.5 × 1 mile side dimensions. There were discernible patterns between field size and the majority crop type as defined by the United States Department of Agriculture (USDA) National Agricultural Statistics Service (NASS) cropland data layer (CDL) classification. In general, larger field sizes occurred where a greater proportion of the land was dedicated to agriculture, predominantly in the U.S. Wheat Belt and Corn Belt, and in regions of irrigated agriculture. The results were validated by comparison with field boundaries manually digitized from Landsat 5 and Google-Earth high resolution imagery. The validation was undertaken at 48 approximately 7.5 × 7.5 km sites selected across a gradient of field sizes in each of the top 16 harvested cropland areas in U.S. states that together cover 76% of harvested U.S. cropland. Conventional per-pixel confusion matrix based measures that assess pixel level thematic mapping accuracy, and object extraction accuracy measures, were derived. The overall per-pixel crop field classification accuracy was 92.7% and the overall crop field producer's and user's accuracies were 93.7% and 94.9%. Comparing all the reference and extracted field objects, 81.4% were correctly matched and the extracted field sizes were on average underestimated by 1.2% relative to the reference field objects.

## 1. Introduction

The spatial distribution of agricultural fields is a fundamental description of rural landscapes (White & Roy, 2015) and is related to a number of ecological factors including habitat fragmentation, biodiversity, cropland species diversity (Geiger et al., 2010; Green, Cornell, Scharlemann, & Balmford, 2005; Krebs, Wilson, Bradbury, & Siriwardena, 1999), the incidence of disease pathogens and pests (Margosian, Garrett, & Hutchinson, 2009), and the regulation of agricultural nutrient, herbicide and pesticide flows (Martin, 2011). Field sizes are indicative of the degree of agricultural capital investment, mechanization and labor intensity, and information on the size of fields is needed to plan and understand these factors, and can help the allocation of agricultural resources such as water, fertilizer, herbicide, and farming equipment (Anderson, Allen, Morse, & Kustas, 2012; Johnson, 2013;

Kuemmerle et al., 2013; Rudel et al., 2009). In many locations, field sizes are increasing due to agricultural intensification as farmers seek to maximize profit and reduce risk through larger agricultural enterprises, with ecological and biogeochemical consequences that require field size information to assess (White & Roy, 2015).

Research to use satellite data for agricultural monitoring has an established heritage (Bauer, Hixson, Davis, & Etheridge, 1978; Duveiller & Defourny, 2010; Moulin, Bondeau, & Delecolle, 1998; Ozdogan, 2010; Wardlow & Egbert, 2008; Whitcraft, Becker-Reshef, & Justice, 2015). However, research on extracting field boundaries and detecting fields has been relatively limited and typically has involved visual identification and manual digitization of field boundaries. In the United States, field boundaries digitized manually from a variety of airborne remote sensing sources are used by the United State Department of Agriculture (USDA) (Boryan, Yang, Mueller, & Craig, 2011), but they are not publically available since the 2008 Food Conservation and Energy Act (U.S. Department of Agriculture, 2008). Satellite land cover classifications that include agricultural classes, such as the United States

\* Corresponding author.
*E-mail addresses:* lin.yan@sdstate.edu (L. Yan), david.roy@sdstate.edu (D.P. Roy).

Geological Survey (USGS) National Land Cover Database (NLCD) (Homer et al., 2015) and the USDA National Agricultural Statistics Service (NASS) crop data layer (CDL) (Johnson & Mueller, 2010), are per-pixel raster classification products that do not define field objects. Recently, a global field size dataset was developed by spatial interpolation of crowd-sourced categorizations of Google-Earth images into "very small", "small", "medium" and "large" field size categories (Fritz et al., 2015). However, although this dataset provides a useful synoptic and qualitative global assessment of field sizes, it contains only ordinal scale field size information and its quality is limited by the small number (13,963) of global samples used (Fritz et al., 2015).

This paper describes the refinements of a recently published algorithm to extract agricultural crop fields from Landsat time series (Yan & Roy, 2014). The refined algorithm integrates a variety of computer vision based image processing techniques; it requires no training data and no human interactions, and is sufficiently computationally efficient and structured to be scalable to continental application. The refined algorithm is applied to one year of Landsat 5 Thematic Mapper (TM) and Landsat 7 Enhanced Thematic Mapper plus (ETM+) data for all of the conterminous United States (CONUS). For the first time, spatially explicit CONUS field size maps and derived information are presented.

The Landsat data and then algorithm refinements are first described. The algorithm was demonstrated previously using five years of Landsat 7 ETM+ data and coherent fields were shown to be extracted with limited errors compared to contemporaneous USDA CDL classifications (Johnson & Mueller, 2010) over three 150 × 150 km regions located in Texas, California and South Dakota (Yan & Roy, 2014). In this paper, the field extraction algorithm was refined to incorporate the CDL to reduce commission errors. The algorithm was applied to one year of Landsat 5 and 7 data to reduce ambiguity due to crop rotations that can occur between years (Plourde, Pijanowski, & Peki, 2013) and to reduce the likelihood of physical field boundary changes that will increase when more years of data are used (Yan & Roy, 2014). Other refinements were also made to improve the algorithm's robustness for CONUS-wide application. Spatially explicit field extraction results and histograms are shown for all the CONUS and in more detail for the state of Iowa that has field distributions that are representative of much of the CONUS. The extracted fields are validated by comparison with field boundaries manually digitized from 48 Landsat 5 TM and Google-Earth 7.5 × 7.5 km subsets selected across the CONUS 16 states with the greatest documented harvested cropland areas. Conventional per-pixel accuracy classification statistics and quantitative object extraction accuracy statistics are presented. The paper concludes with a discussion of the implications of this research and recommendations for future research.

## 2. Data

### 2.1. Landsat data

Landsat data sensed December 2009 to November 2010 were used. Multi-temporal Landsat data were used to ensure sufficient opportunities for cloud-free, non-missing and atmospherically uncontaminated surface observations and to capture variability in the state of the vegetation needed for reliable field extraction (Yan & Roy, 2014). As suggested by previous studies, Landsat 5 TM and 7 ETM+ data, which nominally sense the same location 8-days apart, were used rather than data from a single Landsat to increase the availability of cloud free surface observa-

tions (Kovalskyy & Roy, 2013). A total of 6837 Landsat 7 ETM+ and 6829 Landsat 5 TM scenes processed to Level 1T were used. The Level 1T data processing includes radiometric correction, systematic geometric correction, precision correction using ground control, and the use of a digital elevation model to correct parallax error due to local topographic relief with a CONUS geolocation error less than 30 m (Lee, Storey, Choate, & Hayes, 2004).

Gridded atmospherically corrected Landsat mosaics of the conterminous United States (CONUS) were generated using the Web Enabled Landsat Data (WELD) processing system (Roy et al., 2010). The WELD products are designed to provide consistent data that can be used to derive land cover and geo-physical and bio-physical products. The WELD data have been used previously for large area time series based land cover and change mapping applications (Boschetti, Roy, Justice, & Humber, 2015; Egorov, Hansen, Roy, Kommareddy, & Potapov, 2015; Hansen et al., 2011; Hansen et al., 2014; Yan & Roy, 2015). The WELD products are defined in the Albers equal area projection in 5000 × 5000 30 m pixel WELD tiles, and in this study 362 WELD tiles were processed. The reflectance band data were converted to surface reflectance using the Landsat Ecosystem Disturbance Adaptive Processing System (LEDAPS) code (Masek et al., 2006) that uses aerosol characterizations derived independently from each Landsat acquisition and assumes a fixed continental aerosol type and uses ancillary water vapor data. Weekly WELD composites for 52 weeks from week 49 of 2009 to week 48 of 2010 were used. The compositing algorithm used to generate the weekly data is based on the maximum NDVI algorithm (Roy et al., 2010). Adjacent pixels may be selected from either Landsat 5 or 7 data sensed in the same week and so may be sensed one day apart. The surface reflectance for the green (0.53–0.61 μm), red (0.63–0.69 μm), near-infrared (0.78–0.90 μm) and two mid-infrared (1.55–1.75 μm and 2.09–2.35 μm) Landsat bands were used. The shortest wavelength Landsat blue (0.45–0.52 μm) band was not used because the LEDAPS atmospheric correction is considerably less reliable than for the other Landsat reflective wavelength bands (Ju, Roy, Vermote, Masek, & Kovalskyy, 2012). The per-band radiometric saturation status and the two cloud mask values stored in the WELD data (Roy et al., 2010) were used to remove saturated and cloud contaminated pixels.

### 2.2. Cropland Data Layer

The United States Department of Agriculture (USDA) National Agricultural Statistics Service (NASS) Cropland Data Layer (CDL) for 2010 was obtained from the CDL web site (http://nassgeodata.gmu.edu/CropScape/). The CDL is generated annually using moderate resolution satellite imagery and extensive agricultural ground truth via a supervised non-parametric classification approach and defines about 110 land cover and crop type classes at 30 m (Boryan et al., 2011; Johnson & Mueller, 2010). The 2010 CDL was used in this study to help identify agricultural regions and so provide more direct identification of crop fields. This is needed in particular for this CONUS study as arable agriculture can be hard to discriminate from pasture and other grasslands using Landsat data (Johnson, 2013; Müller, Rufin, Griffiths, Barros Siqueira, & Hostert, 2015; Wardlow & Egbert, 2008). For 2010 the overall CONUS CDL classification accuracy is reported as 84.3% and the major field crops have 85% to 95% classification accuracies (Johnson, 2013). The CDL is defined in the same Albers Equal Area conic projection as the WELD data.

## 3. Field extraction

### 3.1. Overview

The field extraction algorithm requires Landsat 30 m time series in order to capture spectral differences between crop and non-crop phenologies and to reduce the influence of missing, shadowed and atmospherically contaminated satellite observations. The methodology is described and illustrated in detail in Yan and Roy (2014) and can be summarized by five steps: 1) Maps of the probability of crop agriculture and crop field edge

presence are generated from the Landsat time series to provide spatially explicit crop field identification information; 2) A variational region-based geometric active contour (VRGAC) (Chan & Vese, 2001) segmentation method is applied to the two probability maps to derive candidate crop field objects; 3) A watershed algorithm (Bleau & Leon, 2000) is applied to decompose connected candidate crop field objects belonging to multiple fields into coherent isolated fields; 4) A geometry-based algorithm is used to detect and associate parts of circular fields together; 5) The field objects are refined by independent application of a two-pixel dilation and then a one-pixel erosion morphological filter (Serra, 1988) to each extracted field object.

The following refinements were made to the field extraction methodology described in Yan and Roy (2014): 1) Landsat 5 and 7 weekly atmospherically corrected WELD data were used rather than just Landsat 7 weekly WELD top of atmosphere data; 2) maps that describe crop field edge linearity and edge saliency were used rather than a single edge intensity map; 3) The USDA NASS CDL was used to provide a 30 m binary harvested crop mask to replace the crop field probability map used in the original methodology; 4) The VRGAC segmentation was refined to be more robust to within-field spectral variability including the use of new checks for interior field boundary presence and field compactness; 5) Adaptive parameterization was used for bottleneck detection in morphological decomposition of field objects. Fig. 1 illustrates the processing flow of the refined methodology, and Fig. 2 illustrates the results of its application to a $500 \times 500$ 30 m pixel subset that includes a variety of crop fields with different crop types and spatial characteristics.

### 3.2. Edge intensity map generation

An edge intensity map is first generated (Fig. 2c) that is similar to the results of a contrast edge enhancement but enhances edges with high NDVI contrast. It is defined considering at each pixel location the 52 weeks of eight adjacent pixel NDVI and reflectance values as:

$$I_{edge}(i,j) = \frac{\sum_{week=1}^{n} e_{week}(i,j)}{\sum_{week=1}^{n} (NDVI_{week}(i,j))^2} \tag{1}$$

where

$$e_{week}(i,j) = (NDVI_{week}(i,j))^2 \cdot \frac{\sum_{k=1}^{8} d^{\rho}_{week,k}(i,j) \cdot w_k \cdot w^{day}_{week,k}}{\sum_{k=1}^{8} w_k \cdot w^{day}_{week,k}} \cdot \frac{\sum_{k=1}^{8} d^{NDVI}_{week,k}(i,j) \cdot w_k}{\sum_{k=1}^{8} w_k}$$

$$d^{\rho}_{week,k}(i,j) = \sqrt{\sum_{\lambda \in 2,3,4,5,7} (\rho_{week,\lambda}(i,j) - \rho_{week,\lambda}(i+x(k), j+y(k)))^2}$$

$$d^{NDVI}_{week,k}(i,j) = |NDVI_{week}(i,j) - NDVI_{week}(i+x(k), j+y(k))|$$

$$x(k=1\ldots8) = \{0, -1, -1, -1, 0, 1, 1, 1\}$$

$$y(k=1\ldots8) = \{1, 1, 0, -1, -1, -1, 0, 1\}$$

$$w(k=1\ldots8) = \{1, \sqrt{2}/2, 1, \sqrt{2}/2, 1, \sqrt{2}/2, 1, \sqrt{2}/2\}$$

$$w^{day}_{week,k}(i,j) = \left(\frac{1}{|day_{week}(i,j) - day_{week}(i+x(k), j+y(k))| + 1}\right)^4$$

where $I_{edge}(i,j)$ is the edge intensity image, and $d^{\rho}_{week,k}(i,j)$ and $d^{NDVI}_{week,k}(i,j)$ provide measures of the reflectance-based and NDVI-based Euclidean distance respectively of a pixel located in the weekly WELD product for a given *week* at pixel location $(i, j)$ with respect to pixel $k$ located in any of up to eight adjacent pixels defined by offsets $x(k)$, $y(k)$. If there are no data at $(i, j)$ or no adjacent pixels with data, denoted by a fill value in the weekly WELD products, then (1) is not defined. This formulation is similar to the crop field edge presence probability estimation described in Yan and Roy (2014) but with the added refinement of $w^{day}_{week,k}(i,j)$ that normalizes for differences in the acquisition dates of neighboring pixels that occur as both Landsat 5 and 7 data are used. The formulation of $w^{day}_{week,k}(i,j)$ is defined such that if a neighboring pixel has the same acquisition date then the weight is one, but if the date is different by one day then the weight is much smaller (1/16). In addition, the square of $NDVI_{week}(i,j)$ is used to weight the NDVI as this was found to be useful to emphasize harvested crop field edges that have short growing periods.

The edge intensity image is also normalized to fall into the range [0, 1] as:

$$\hat{I}_{edge}(i,j) = \begin{cases} 1, & \text{if } I_{edge}(i,j) > I_1 \\ \dfrac{I_{edge}(i,j) - I_2}{I_1 - I_2}, & \text{if } I_2 \leq I_{edge}(i,j) \leq I_1 \\ 0, & \text{if } I_{edge}(i,j) < I_2 \end{cases} \tag{2}$$

where $\hat{I}_{edge}(i,j)$ is the normalized edge intensity image at pixel location $(i, j)$. Edge intensity image values $>I_1$ are likely edge members (normalized value set to 1), values in the range $[I_2, I_1]$ are possible edge members (normalized values set between 0 and 1), and values $<I_2$ are not likely edge members (normalized value set to 0). In this study, $I_1$ and $I_2$ were set to 4.0 and 2.0 respectively, which are aggressively low thresholds to ensure weak edges are not missed. These two values were determined by manual inspection of the edge intensity values of weak field boundaries at multiple CONUS locations.
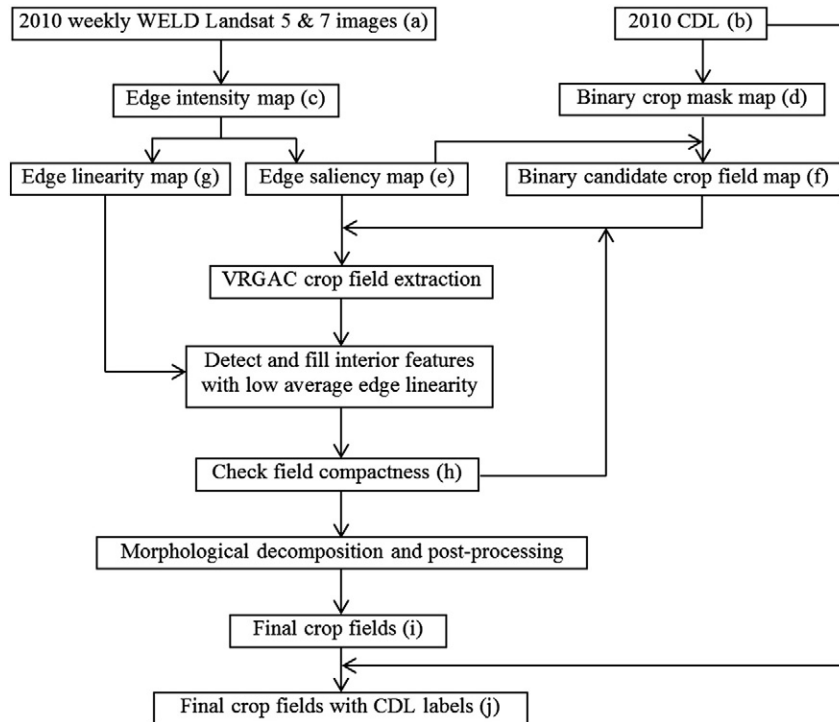
**Fig. 1.** Processing flow of the refined automated field extraction methodology; results for the letters in parentheses are illustrated in Fig. 2.

Fig. 3 illustrates a detailed example of the edge intensity image (Fig. 3a) and the normalized edge intensity image (Fig. 3b) and also illustrates the corresponding edge linearity and saliency maps whose generations are explained below.

### 3.3. Edge linearity and saliency map generation

The edge intensity map is used to generate maps that quantify the degree of straightness of the intensity edges (edge linearity) and also the degree to which intensity edges stand out locally relative to their neighbors (edge saliency). The edge linearity and saliency are derived only if a pixel has $\hat{I}_{edge}(i,j) > 0$. The edge saliency is input to the VRGAC and the edge linearity is used to refine the VRGAC output (Fig. 1).

The motivation for the edge linearity and saliency map generation reflects computer vision research that is focused on understanding how humans correctly interpret visual images (Marr, 1982). Several computer vision edge and object extraction approaches model observations that human perception of an oriented stimulus is influenced by the presence of other similar surrounding stimuli, and that only a single edge at a time is interpreted as passing through any given point in an image (Field, Hayes, & Hess, 1993; Geisler, Perry, Super, & Gallogly, 2001; Papari & Petkov, 2011; Ramachandra & Mel, 2013). In particular, the response of the human visual system to an oriented stimulus is reinforced from surrounding stimuli that are collinear with the central stimulus and inhibited by other stimuli in the direction orthogonal to the edge direction (Papari & Petkov, 2011). For the purposes of this study, the oriented stimuli of interest are field boundaries.

Previous field extraction research suggested that it is useful to detect and include linear field boundaries even though they may be weakly detected (Rydberg & Borgefors, 2001). Detection weakness occurs because the field boundaries are often narrower than the Landsat 30 m pixel dimension (Ji, 1996; White & Roy, 2015) and when this occurs, neighboring fields with similar-phenology may not provide high edge intensity map values (Yan & Roy, 2014). In addition, field boundaries in regions of persistent cloud may be obscured and so have lower edge intensity values, particularly if the cloud obscuration period coincided with the peak of the growing season.

In this study, field boundaries are assumed to be locally continuous and either straight or curved to reflect the mechanized nature of most CONUS farming. Fields with straight side boundaries smaller than length $(l/2 + 1)$ pixels are assumed to not occur, or if they occur they will not be detected. The parameter $l$ was set to 6 pixels so that fields with boundaries shorter than 4 pixels (i.e. about 120 m) will not be detected. It was found that using smaller $l$ values was unreliable as within-field variations were increasingly detected as possible field boundaries and because of the difficulties of defining a line over distances shorter than 4 pixels.

#### 3.3.1. Edge orientation derivation

Before the edge linearity or saliency can be computed, the edge orientation, i.e., the direction relative to Cartesian image row and column coordinates, must be defined. Fig. 3b depicts the optimal edge direction (red vectors) for each pixel relative to the neighboring normalized edge intensity values and Fig. 4 illustrates the optimal edge direction search process that is undertaken by examination of the normalized intensity values where $\hat{I}_{edge}(i,j) > 0$. A diametral spatial search for different radial directions defining a circle centered on $(i,j)$ is undertaken (Fig. 4a). In each direction (Fig. 4b), search lines from $(l/2 + 1)$ to $(l + 1)$ pixels that pass through $(i,j)$ and that are composed of consecutive pixels with $\hat{I}_{edge}(i,j) > 0$ are considered. For clarity, the adjacent pixels in a vertical search are illustrated in Fig. 4b; for non-vertical or non-horizontal search directions, the adjacent

(a) 2010 weekly WELD L57 images

(b) 2010 CDL

(c) Edge intensity map

(d) Binary crop mask map (white = crop)

(e) Edge saliency map

(f) Binary candidate crop field map with 2 pixel buffered edge (gray)
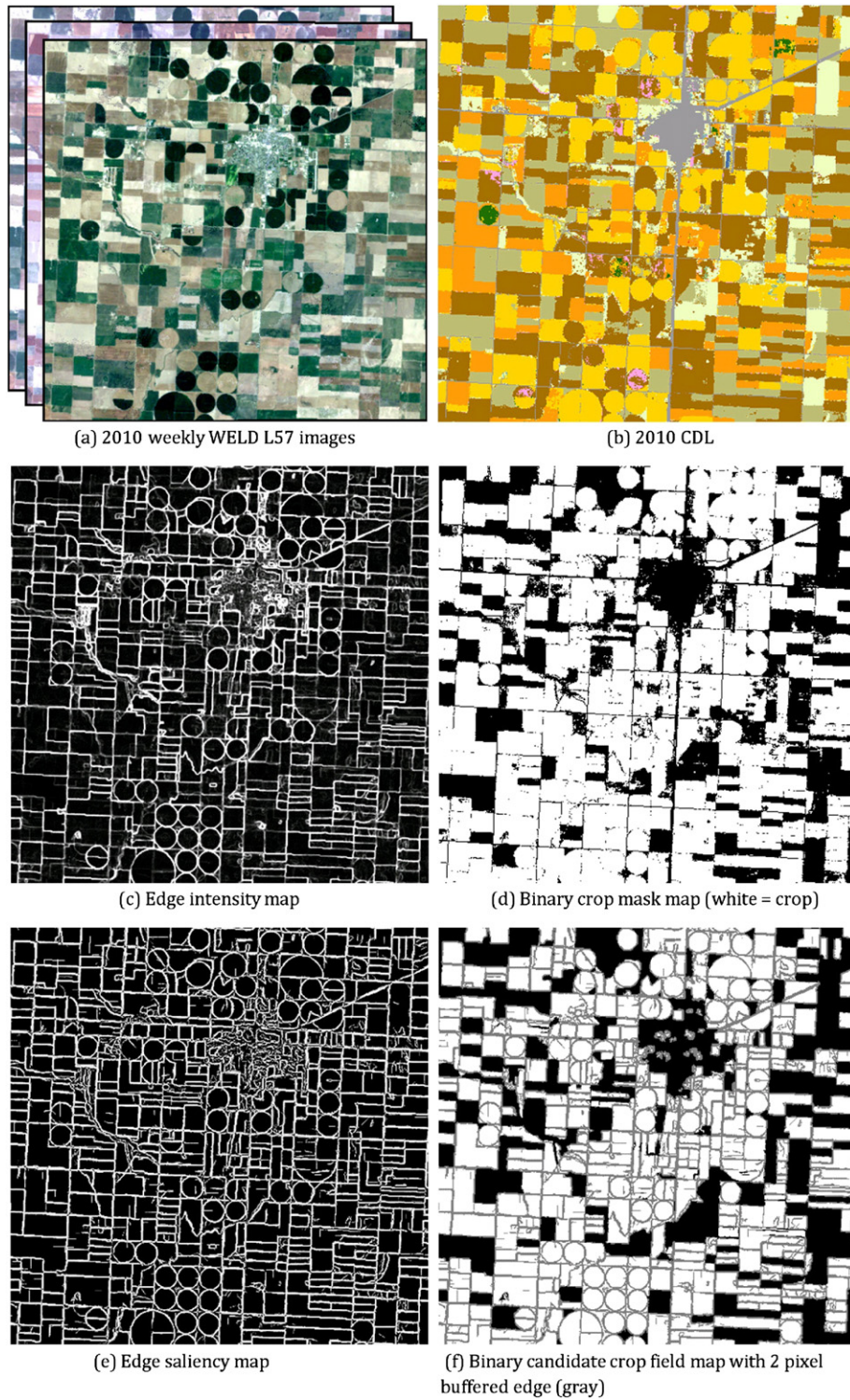
**Fig. 2.** Illustration of several of the steps in the refined automated field extraction methodology processing flow (Fig. 1) for a 500 × 500 30 m pixel region surrounding Scott City, Kansas, USA. There were 438 extracted fields.

pixels along the closest approximation to the straight line through $(i, j)$ are defined using a conventional Bresenham line algorithm (Bresenham, 1965).

The optimal edge direction is derived from the search process (Fig. 4) as the one where the metric $\hat{si}$ is the maximum over all the different searches (radial directions and search lines in each radial direction):

$$\hat{si} = \sum_{k=1}^{n} \hat{I}_{edge}(i_k, j_k) \tag{3}$$

(g) Edge linearity map

(h) Extracted crop fields that pass compactness check

(i) Decomposed and post-processed final crop fields colored randomly to illustrate they are separate objects (black = not crop fields)

(j) Final crop fields shown with margins of each eroded by one pixel and colored with majority CDL labels for clarity.

**Fig. 2** (*continued*).

where $\hat{si}$ is the summed normalized edge intensity of the consecutive set of $n$ pixels along the search line referenced for convenience as $\{(i_k j_k)|k=1...n\}$, and $n$ can vary from $(l+1)/2$ to $(l+1)$ pixels (Fig. 4b). Th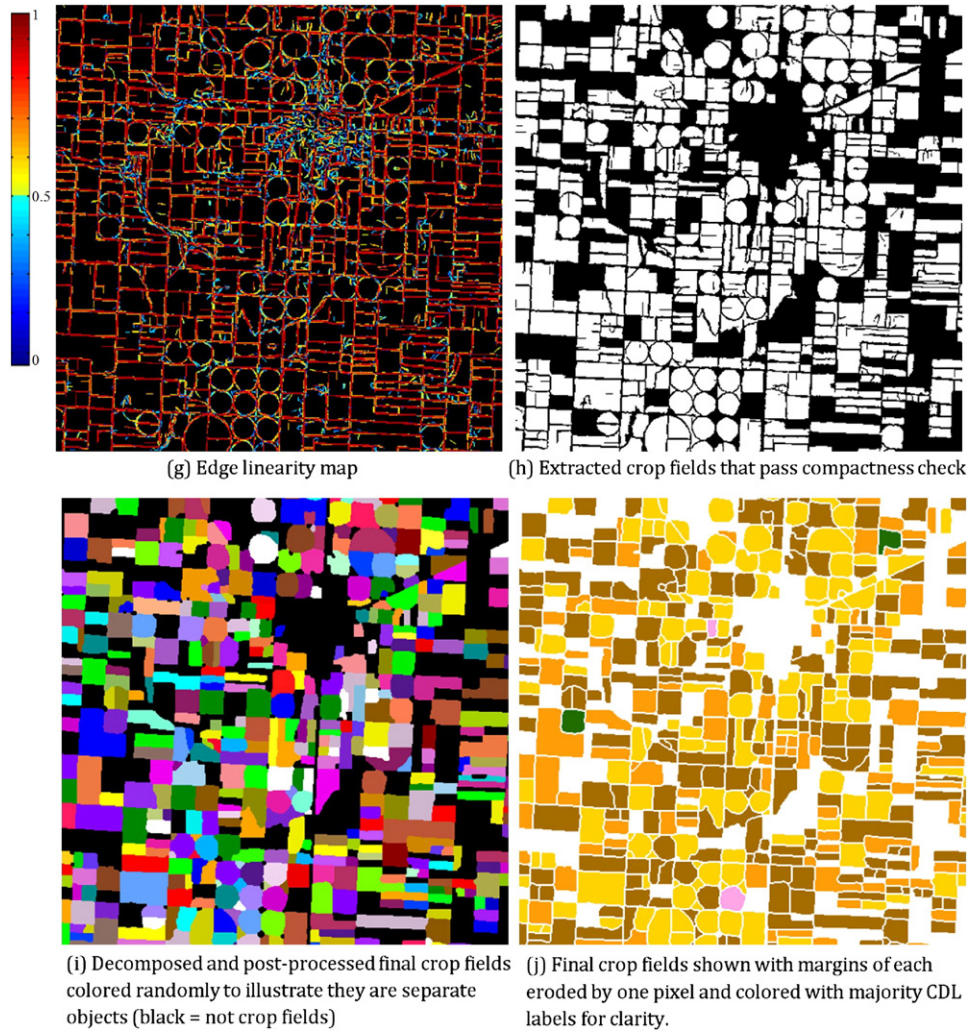e optimal edge direction, the number of pixels in the corresponding optimal search line, and the value of $\hat{si}$, denoted $\alpha_{opt}(i,j)$, $n_{opt}(i,j)$ and $\hat{si}_{opt}(i,j)$ respectively, are recorded. Occasionally there are "tied" cases when there are more than one $\hat{si}$ maxima; when this occurs another measure $si_w$ is computed:

$$si_w = \frac{\sum\limits_{k=1}^{n} I_{edge}(i_k, j_k) \cdot w_k^{similarity} \cdot w_k^{dist}}{\sum\limits_{k=1}^{n} w_k^{similarity} \cdot w_k^{dist}}$$

$$w_k^{similarity} = \frac{1}{1 + |I_{edge}(i_k, j_k) - I_{edge}(i,j)|}$$

$$w_k^{dist} = \frac{1}{1 + |k - k_o|}$$

(4)

where $si_w$ is derived in a weighted manner from the edge intensity image and $k_o$ is the pixel index of $(i,j)$ that falls on the search line. The values of $\alpha_{opt}(i,j)$, $n_{opt}(i,j)$ and $\hat{si}_{opt}(i,j)$ are then defined as before but from the search with the maximum $si_w$. Note that $si_w$ rarely has tied maximal values as it is derived from the intensity edge image and not the normalized version that has a smaller and bounded dynamic range.

Finally, all the $\alpha_{opt}(i,j)$ values are compared with their neighboring $\alpha_{opt}$ values to ensure that the orientations are locally consistent. At each pixel location $(i,j)$, the mean intersection angle (defined as an acute angle) between $\alpha_{opt}(i,j)$ and each set of available neighboring $\alpha_{opt}$ values defined from one to no more than $l$ consecutive pixels in direction $\alpha_{opt}(i,j)$ is derived. If the minimum mean intersection angle is >15°, then local consistency is considered to be lost and $\alpha_{opt}(i,j)$ is removed from consideration. This 15° threshold was set conservatively as nearly twice the angle subtended by a small 0.25 mile radius circular field over a distance of $(l+1)$ 30 m pixels. In our previous research, center-pivot irrigation circular fields with
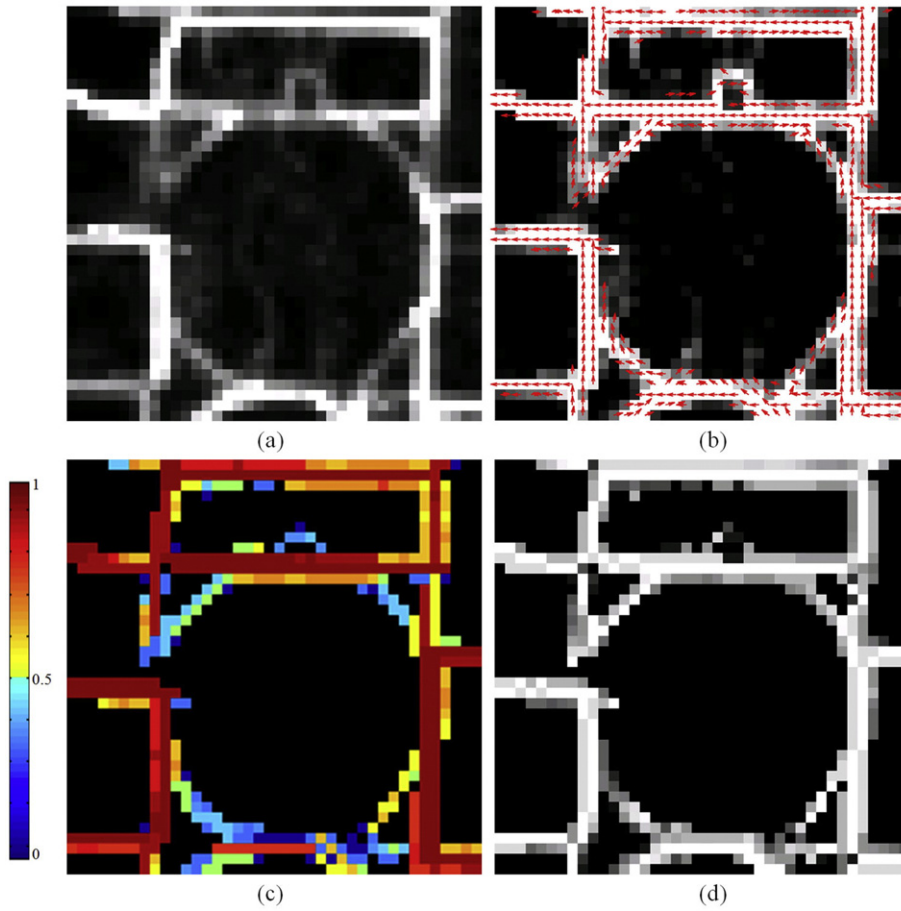
**Fig. 3.** Example of edge linearity and saliency map generation over straight and circular field boundaries for a 40 × 40 30 m pixel subset located near the south-east corner of the Fig. 2 image, (a) edge intensity map, (b) normalized edge intensity map overlain with estimated optimal edge direction vectors shown in red (see text for details), (c) edge linearity map, (d) edge saliency map.
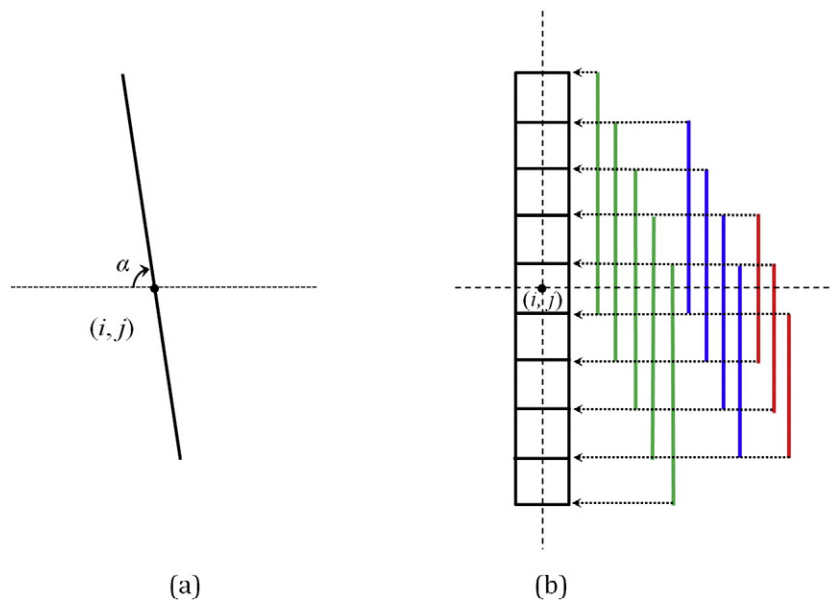


**Fig. 4.** Illustration of the optimal edge direction search process. (a) A diametral spatial search is undertaken for different radial directions defined as the angle $\alpha(i,j)$ with the image x-axis, (b) in each radial direction search, lines from $(l/2 + 1)$ to $(l + 1)$ pixels that pass through $(i,j)$ and are composed of consecutive pixels with $l_{edge}(i,j) > 0$ are considered; in this example, search lines for $l = 4$ pixels are illustrated that provides 12 possible search lines (colored) from three to five pixels in length.

radii of 390 m (about 0.25 mile) and 790 m (about 0.5 mile) were detected (Yan & Roy, 2014) that corresponded to the radii required to irrigate quarter section (0.5 × 0.5 mile) and full section fields (1 × 1 mile) common in the U.S. (Pitts & Badhwar, 1980).

### 3.3.2. Edge linearity derivation

The edge linearity is defined by consideration of the optimal edge direction pixel values for sequences of consecutive adjacent pixels that pass through $(i, j)$ in the direction defined by $\alpha_{opt}(i, j)$ and searching in a similar manner as Fig. 4b. First, for each sequence of $n$ pixels varying from one to $(2 l + 1)$ pixels, the following collinearity measure is derived:

$$c(i, j) = \sum_{k=1}^{n} \cos\left(\left|\alpha_{opt}(i_k, j_k) - \alpha_{opt}(i, j)\right|\right) \tag{5}$$

where $c(i, j)$ is a collinearity measure bounded $[0, 2l + 1]$, $\alpha_{opt}(i_k, j_k)$ define the optimal edge orientations derived at pixel location $(i, j)$ at $n$ consecutive pixel locations $\{(i_k j_k) | k = 1...n\}$ and the search is terminated if $\alpha_{opt}(i_k, j_k)$ is not defined or if more than $(2l + 1)$ pixels are examined. Then the edge linearity is defined:

$$L_{edge}(i, j) = \frac{c_{\max}(i, j)}{2l + 1} \tag{6}$$

where $L_{edge}(i,j)$ is the edge linearity at pixel $(i, j)$, the denominator is included so that $L_{edge}(i,j)$ has a value in the range $[0, 1]$, and $c_{max}$ is the maximum of the collinearity measure (5) derived over the different sequences of consecutive adjacent pixels that pass through $(i, j)$. Fig. 3c shows detailed example edge linearity results. The straightest and longest connected edges have the greatest linearity values. The curved edges have lower values because they are not straight. If circular fields are sufficiently large then the degree of linearity of the field edge will still provide useful information.

### 3.3.3. Edge saliency derivation

The edge saliency models the response of the human visual system to an oriented stimulus that is reinforced from surrounding stimuli that are collinear with the central stimulus and inhibited by other stimuli in the direction orthogonal to the edge direction (Papari & Petkov, 2011). Inhibition is quantified using a search considering different sets of consecutive pixels progressively further away from $(i, j)$ in the orthogonal direction to $\alpha_{opt}(i, j)$ until a pixel with an edge intensity value no less than $I_{edge}(i,j)$ occurs or $(v + 1)$ pixels are considered; this search is similar to the search with $l$ as illustrated in Fig. 4b. The parameter $v$ was set as twice $(l/2 + 1)$, i.e. $v = 8$ pixels, to reduce inhibition from homogenous regions within this distance. Recall that fields with straight side boundaries smaller than length $(l/2 + 1)$ pixels will not be detected.

The edge saliency $S_{edge}(i,j)$ is defined as:

$$S_{edge}(i, j) = \begin{cases} \dfrac{s\hat{i}_{opt}(i, j)}{l + 1} \cdot \dfrac{n_{opt}(i, j)}{l + 1} \cdot \dfrac{n_{\perp opt}(i, j)}{v + 1}, & \text{if} \quad L_{edge}(i, j) < 0.5 \\[2ex] \min\left(\dfrac{s\hat{i}_{opt}(i, j)}{l + 1} \cdot \dfrac{c_{\max}(i, j)}{l}, 1\right) \cdot \dfrac{n_{opt}(i, j)}{l + 1} \cdot \dfrac{n_{\perp opt}(i, j)}{v + 1}, & \text{if} \quad L_{edge}(i, j) \geq 0.5 \end{cases} \tag{7}$$

where $\frac{s\hat{i}_{opt}(i,j)}{l+1}$, $\frac{n_{opt}(i,j)}{l+1}$ and $\frac{n_{\perp opt}(i,j)}{v+1}$ define the normalized edge intensity, reinforcement and inhibition terms, respectively, and the denominators (expressed in terms of the $l$ and $v$ search parameters) are included so that the terms, and therefore the edge saliency, are defined in the range $[0, 1]$. The variables $s\hat{i}_{opt}(i, j)$, $n_{opt}(i, j)$ and $c_{max}(i, j)$ are, respectively, the summed normalized edge intensity (3), the number of pixels defining the optimal edge direction search line, and the maximum of the collinearity measure (5) calculated from consecutive pixels in the optimal edge direction. The variable $n_{\perp opt}(i,j)$ is the maximum number of consecutive pixels with an edge intensity value less than $I_{edge}(i, j)$ found searching orthogonally to the optimal edge direction.

The two cases to derive the edge saliency (7) are used to boost the edge saliency values for edges with relatively high linearity defined as $L_{edge}(i, j) \geq 0.5$; the term $\frac{c_{\max}(i,j)}{l}$ is always greater than unity when $L_{edge}(i, j) \geq 0.5$ such that it boosts the normalized edge intensity term $\frac{s\hat{i}_{opt}(i,j)}{l+1}$ to up to 1. This is needed as the normalized edge intensity can have low values (Fig. 3b) even for long straight edges with high linearity values (Fig. 2g, Fig. 3c). Fig. 3d shows detailed example edge saliency results. High saliency values occur not only where there are straight and long edges with high linearity values (Fig. 3c) but also for portions of the circular field edges that lie furthest from the bounding straight edges, and much of the within-field noise is removed. This example illustrates why the edge saliency map rather than the normalized edge intensity map is used as an input to the VRGAC field extraction (Fig. 1). The normalized edge intensity values are quite variable for the reasons discussed at the beginning of this section, whereas the saliency values are relatively enhanced along real edge locations that are not close to other edges. The edge saliency is not defined if $\hat{I}_{edge}(i, j) = 0$ or if $\alpha_{opt}(i, j)$ is not defined at pixel location $(i, j)$. The edge saliency is defined in the range $[0, 1]$, and with the parameters $l = 6$ and $v = 8$, typically field boundaries have edge saliency values >0.5.

### 3.4. Binary crop mask and candidate binary candidate crop field map generation

The USDA NASS CDL (Fig. 2b) is used to help identify agricultural regions and so provide more direct identification of crop fields. The 2010 CDL was used, rather than other CDL years, to best match the December 2009 to November 2010 Landsat data acquisition period. Although previous research has indicated a visual correspondence between the CDL data and extracted field objects (Yan & Roy, 2014, Yang, Wilson, & Wang, 2014), the CDL does not define field objects.

The CDL is filtered to provide a 30 m binary harvested crop mask by assigning all the agricultural CDL classes as crop pixels and the remainder as non-crop pixels (Fig. 2d). A binary candidate crop field map is then generated from the binary crop mask using the edge saliency map to reduce sensitivity to CDL classification errors. A straightforward process is used. All the connected neighboring pixels with $S_{edge} = 0$ (i.e., black in Figs. 2e and 3d) are located, and those with a majority of binary crop mask pixels labeled as crop are considered as candidate crop field objects. A 2-pixel buffer

around each binary candidate crop field is also defined, labeling in the buffer only pixels with $S_{edge} > 0$ (shown as gray in Fig. 2f). This buffer is used in the VRGAC field extraction.

## 3.5. VRGAC field extraction

Crop fields are extracted by application of the VRGAC segmentation algorithm to the edge saliency map and using the binary candidate crop field map to initialize the VRGAC (Fig. 1). The VRGAC is well established (Chan & Vese, 2001) and requires only a small number of parameters to iteratively generate a segmentation with control over the smoothness of the segment boundaries and segmentation noise. A level set function approach is used that enables numerical computations on a Cartesian image grid without having to parameterize segment curve and surface properties that can be particularly complex to parameterize (Osher & Sethian, 1988). The level set function is a two dimensional matrix with each element corresponding to a pixel location and with values storing the spatial distance to the closest object boundary. Signed distances are stored so that locations inside an object are negative and increase in value for locations closer to the object boundary, and locations outside of the object have positive values. Object boundaries are defined be zero-crossing locations in the level set function. This is illustrated in detail in Yan and Roy (2014) for field objects extracted from Landsat data.

The VRGAC implementation was revised slightly from that used in (Yan & Roy, 2014) to reflect the different inputs as:

$$\phi(i,j)_{n+1} = \phi(i,j)_n + \delta_\varepsilon(\phi(i,j)_n) \cdot (\mu \cdot \kappa(i,j)) + S_{edge}(i,j) - c \qquad (8)$$

where $\phi(i,j)$ is the level set function composed of signed distances at each pixel location $(i,j)$ derived initially from the binary candidate crop field map (Section 3.4), and $\phi(i,j)_{n+1}$ is the updated version of $\phi(i,j)_n$, $\delta_\varepsilon$ is an approximated *Delta* function, $\kappa(i,j)$ is the curvature map of $\phi(i,j)_n$ (Caselles, Catte, Coll, & Dibos, 1993; Yan & Roy, 2014), $\mu$ and $c$ are scalar constants that control the segmentation performance, and $S_{edge}(i,j)$ is the edge saliency defined as (7). The *Delta* function $\delta_\varepsilon$ is configured to constrain the update of $\phi$ to an area within 1.5 pixels from the current field object boundaries as described in Yan and Roy (2014). In this implementation, the update of $\phi$ is undertaken only at pixel locations in the binary candidate crop field and the surrounding 2-pixel buffer region (white and gray respectively, Fig. 2f) to prevent field objects from propagating into non-crop field areas (black, Fig. 2f). The constant $\mu$ is applied to $\kappa(i,j)$ to control boundary smoothness and is set as 0.03 (Yan & Roy, 2014). The constant $c$ varies between 0 and 1 and is set as described below. It is used to moderate the edge saliency $S_{edge}(i,j)$ values; larger $c$ increases the likelihood that pixels with low $S_{edge}(i,j)$ are included into field objects, which tends to make the extracted field objects more compact.

The level set function is updated as (8) until a pre-defined stable state is reached. In this study, as previously (Yan & Roy, 2014), the iteration is stopped when less than 0.001% of the signed distance values change over 20 consecutive iterations. The extracted field objects are defined by application of a simple local search and connected neighboring level set function pixels with negative signed distance values are labeled as belonging to the same field object.

Each set of extracted field objects is checked for interior features with low average linearity, and if any are detected they are filled (Section 3.6), and then the compactness of the resulting field objects are quantified (Section 3.7). Fields that are insufficiently compact are presented to the VRGAC as a new version of the candidate crop field map (Fig. 1). This is repeated iteratively; each time $c$ is varied with 0.1 increments from 0.25 to 0.85 to gradually strengthen the smoothening of the field object boundaries, and the fields that are found to be compact are stored. As field boundaries typically have edge saliency values >0.5, iterating c from 0.25 to 0.85 ensures that they are captured. In this way, a total of seven iterations are undertaken, and the final field object extraction is defined by the union of the seven field object extractions (Fig. 2h).

## 3.6. Filling interior features with low average linearity

Previous research has indicated the complexity of agricultural landscapes with interior ditches, hedges, tree lines, weed and grass swards, linear poorly drained depressions, regions of infertile soil, ponds, and narrow tracks (Palmer, Kutser, & Hunter, 2015; Rydberg & Borgefors, 2001; White & Roy, 2015; Yan & Roy, 2014). These kinds of features often cause the extracted fields to be complex and may introduce interior "hole"-like features due to the VRGAC smoothing. The interior holes can be just one pixel wide. They are first identified by a neighborhood search across each extracted field object and then the mean edge linearity $L_{edge}(i,j)$ of their pixels is derived. If the mean edge linearity is less than 0.5, then all the pixels defining the feature are converted into field pixels. This removes non-linear narrow internal features, and removes internal holes such as ponds, and so reduces the potential for subsequent over-segmentation of fields whereby larger fields are incorrectly subdivided into smaller ones. Considering the edge linearity definition (6), a 0.5 linearity is equivalent to a 50% probability of a pixel lying on a $(2l + 1)$ pixel-long linear line, and therefore provides a reasonable threshold.

## 3.7. Field compactness check

Measurement of object compactness is well established and a number of measures have been proposed (Bogaert, Rousseau, Van Hecke, & Impens, 2000; Groom & Schumaker, 1993; Li, Goodchild, & Church, 2013) and applied to satellite data (Chuvieco, 1999; Li & Yeh, 2004). The following measure (Groom & Schumaker, 1993) is used:

$$compactness = \frac{4\sqrt{A}}{P} \qquad (9)$$

where $A$ is the number of pixels defining the object (i.e., the object area) and $P$ is the summed length of the interior and exterior perimeters of the object. This measure is scale-invariant, is bounded from zero (not compact) to one (maximum compactness), and is suitable for two dimensional image rasters as square (rather than circular) objects provide the maximum compactness value. Smaller values occur for irregularly shaped fields and particularly for fields with holes and interior angles greater than 180°. Rather than using a fixed compactness threshold, an area-adaptive

threshold is implemented, and objects with compactness values less than $0.6532-0.0073(\sqrt{A})$ are considered to be insufficiently compact and are further refined by the VRGAC. The parameters 0.6532 and 0.0073 were derived by linear regression of compactness against $\sqrt{A}$ values considering 110 binary candidate field map objects manually selected to cover a range of field shapes and areas. This area-adaptive thresholding ensures that larger field objects are more likely to be considered compact.

Objects further refined by the VRGAC may not be changed and so the aggressive implementation of the area-adaptive compactness threshold is not critical. However, narrow fields that often have small compactness values (Li & Yeh, 2004) may also have low edge saliency values if they are small, and so the VRGAC may merge them with adjacent field objects. To reduce this occurrence, the ratio of an field object's area to the area of the minimum rectangular bounding box around the object (O'Rourke, 1985) is derived, and objects with ratios greater than 0.8 are considered compact and not further refined by the VRGAC. The 0.8 threshold was determined empirically by examining the object area and minimum rectangular bounding box area of binary candidate field map objects with minimum side dimensions less than 4 (i.e. $l/2 + 1$) pixels.

### 3.8. Crop field object morphological decomposition and post-processing

Object extractions may be imperfect with errors that include the incorrect subdivision of larger objects into smaller ones (termed over-split or over-segmentation) and the consolidation of small adjacent objects into larger ones (termed under-split or under-segmentation) (Möller, Birger, Gidudu, & Gläßer, 2013; Persello & Bruzzone, 2010). In the original algorithm implementation (Yan & Roy, 2014), the latter issue was found to be common and was noted as occurring if the boundary between adjacent joining crop fields is indistinct or when a curved boundary just meets, "kisses", the curved or straight boundary of an adjacent field. Consequently, a morphological decomposition algorithm is implemented to decompose the connected segments belonging to multiple fields into isolated fields.

Similarly to the original algorithm (Yan & Roy, 2014), the level set function $\phi(i,j)$ derived from the extracted crop fields that pass the compactness check (Fig. 2h) is used in the decomposition step. A standard watershed method (Bleau & Leon, 2000) is used to find regional minima in the level set function, i.e. to find the regionally most negative signed distance value locations. Candidate field objects with level set functions containing more than one minimum are potential candidates for subdivision. They are decomposed into separate objects if the following condition within a field object occurs:

$$\min|\phi(\text{Skeleton } (m_1, \ m_2))| < \alpha \cdot \min(|\phi \ (m_1)| \ |\phi(m_2)|) \tag{10}$$

where $\phi$ is the level set function derived from the extracted crop fields that pass the compactness check, Skeleton $(m_1, m_2)$ denotes the topological skeleton line (set of two-dimensional image coordinates) connecting two adjacent minima $m_1$ and $m_2$, and $\alpha$ is a coefficient in the range $(0, 1)$ set to 2/3 (Yan & Roy, 2014). The topological skeleton line, also referred to as the medial axis of an object, is the set of all image coordinates occurring inside the object that have more than one closest point on the object's boundary (Lee, 1982). For most field objects, the topological skeleton line is usually not straight. The left hand side of Eq. (10) defines the minimum distance to the boundary from the image coordinate on the topological skeleton line that is closest to an object boundary (which is potentially a "bottleneck" location). The right hand side of Eq. (10) defines the product of $\alpha$ and the smaller distance to the object boundary of $m_1$ and $m_2$. Greater $\alpha$ values result in an increased likelihood of (10) occurring and thus the decomposition into two separate field objects associated with $m_1$ and $m_2$. If $\alpha$ is greater than unity, then decomposition will always occur. In this study, $\alpha$ was implemented as an adaptive threshold to reduce its value (compared with 2/3 originally used), and so reduce the amount of decomposition, except for cases when adjacent circular fields just meet as:

$$\alpha = \begin{cases} 0.5 + 5[\max(0, \quad \text{circularity}(m_1) - 0.9)] & if \quad \phi(m_1) \in [9, 30] \text{ and } \phi(m_2) \notin [9, 30] \\ 0.5 + 5[\max(0, \quad \text{circularity}(m_2) - 0.9)] & if \quad \phi(m_1) \notin [9, 30] \text{ and } \phi(m_2) \in [9, 30] \\ 0.5 + 5[\max(0, \quad \text{circularity}(m_1) - 0.9) + \max(0, \quad \text{circularity}(m_2) - 0.9)] & if \quad \phi(m_1) \in [9, 30] \text{ and } \phi(m_2) \in [9, 30] \\ 0.5 & otherwise \end{cases} \tag{11}$$

where circularity(m) is the two-dimensional correlation coefficient (Taylor, 1990) between a sub-matrix of $\phi$ defined with square dimensions $(2[\phi(m)] + 1) \times (2[\phi(m)] + 1)$ pixels centered at the image location of m, with a level set matrix defined by a perfect circle with diameter of $2[\phi(m)] + 1$ pixels. This type of level set template matching is a commonly used technique for shape recognition (Bresson, Vandergheynst, & Thiran, 2006; Cremers, Rousson, & Deriche, 2007; Tsai, Yezzi, Wells, & Tempany, 2003). The circularity has a value from 0 (no correlation) to 1 (perfect correlation) and so $\alpha$ is usually 0.5, i.e. less than the 2/3 value used in the original implementation (Yan & Roy, 2014) but greater than 0.5 when one or both minima have circularity values greater than 0.9. Thus the adaptive $\alpha$ threshold reduces over-splitting of non-circular field objects. If either of the two minima occur less than 9 pixels (270 m) or more than 30 pixels (900 m) from the object boundary then $\alpha$ is set as 0.5; these distances are several pixels smaller than the smallest and longest circular agriculture field radii observed in Texas, California and South Dakota (Yan & Roy, 2014) and also observed in this CONUS study.

Finally, the extracted field objects are cleaned by application of dilation and erosion morphological filters (Serra, 1988). As in the original paper (Yan & Roy, 2014), first a two-pixel dilation is applied and then a one-pixel erosion is applied to all the field objects together, to produce field boundaries that spatially abut (Fig. 2i). Analysis of the application of the algorithm to the CONUS Landsat data indicated that fields greater in size than 20 pixels (0.018 km²) were sufficiently large to be extracted reliably, but below this size, depending primarily on the field shape, the extraction was less reliable. Consequently, all extracted fields smaller than 20 pixels (0.018 km²) were discarded. Fig. 2j illustrates the CDL-labeled field objects for visualization purposes only. The field extraction results appear visually reliable (e.g., Fig. 2i, j), but should be validated quantitatively.
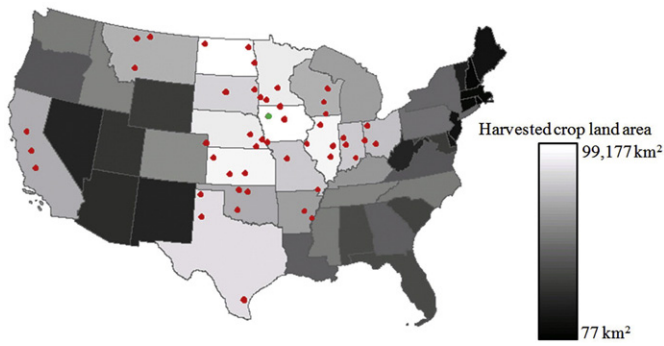
**Fig. 5.** Distribution of the 48 7.5 km × 7.5 km validation sites (3 validation sites × 16 states) superimposed over the CONUS statewise harvested cropland area (2012 USDA Agricultural Census). The validation states are shown by red dots and the green dot shows the location of the Alta, Iowa validation site illustrated in Fig. 13.
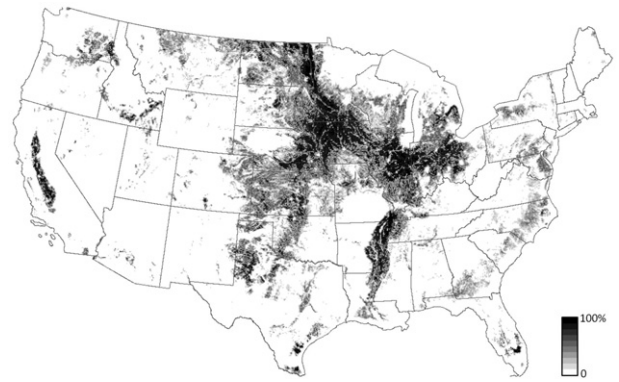


**Fig. 7.** Comparative CONUS 2010 CDL crop percentage map. The crop percentage in 7.5 km × 7.5 km gridcells is shown (grayscale colors, <10% shown in white) with state boundaries in gray. The maximum gridcell percentage value is 98.4%.

## 4. Validation methodology

### 4.1. Validation site sampling

The accuracy of satellite products should be assessed by comparison with higher accuracy independent reference data that are distributed over a range of representative conditions or that are located using a statistical sampling methodology (Justice et al., 2000; Morisette, Privette, & Justice, 2002; Stehman, 2009). In this study the former approach was used as no publically available CONUS map of field size distributions from which to develop a sampling methodology exists.

The following validation site sampling procedure was used. The CONUS was divided into 7.5 km × 7.5 km gridcells in the Albers equal area projection, and each potential validation site was defined by a gridcell. The 7.5 km gridcell dimension was greater than the largest field dimensions reported in the literature that report CONUS long-axis field dimensions as great as 6 km (Connor, Loomis, & Cassman, 2011; Ferguson, Badhwar, Chhikara, & Pitts, 1986). The mean field size in each 7.5 km × 7.5 km gridcell containing more than 50% crop classified CDL pixels and at least 50 extracted fields was computed. The mean gridcell values were ranked in each state and, in each state, the three gridcells containing the minimum,

median and maximum mean field sizes were selected as potential validation sites. Given the large geographic extent of the CONUS and the time consuming nature of the independent reference data generation, 16 states were used to provide 16 × 3, i.e. 48 gridcells where independent reference data were generated (Fig. 5). The 16 states were those with the greatest harvested cropland area (USDA 2012 Census), namely (listed in descending order of harvest cropland area) Iowa, North Dakota, Illinois, Kansas, Minnesota, Nebraska, Texas, South Dakota, Missouri, Indiana, Ohio, Montana, Wisconsin, Oklahoma, California, and Arkansas. These 16 states together cover 76% of the harvested U.S. cropland (USDA 2012 Census) and so we can reasonably expect that the 48 selected sites encompass a range of field size distributions that are representative of the CONUS. The validation sites were defined with straight boundaries and their boundary locations were shifted as needed to ensure that the boundaries only intersected a minority of fields; consequently several validation sites encompassed state boundaries.

### 4.2. Independent reference data generation

Independent reference data that define the locations and boundaries of crop fields were defined by an interpreter using Landsat 5 TM
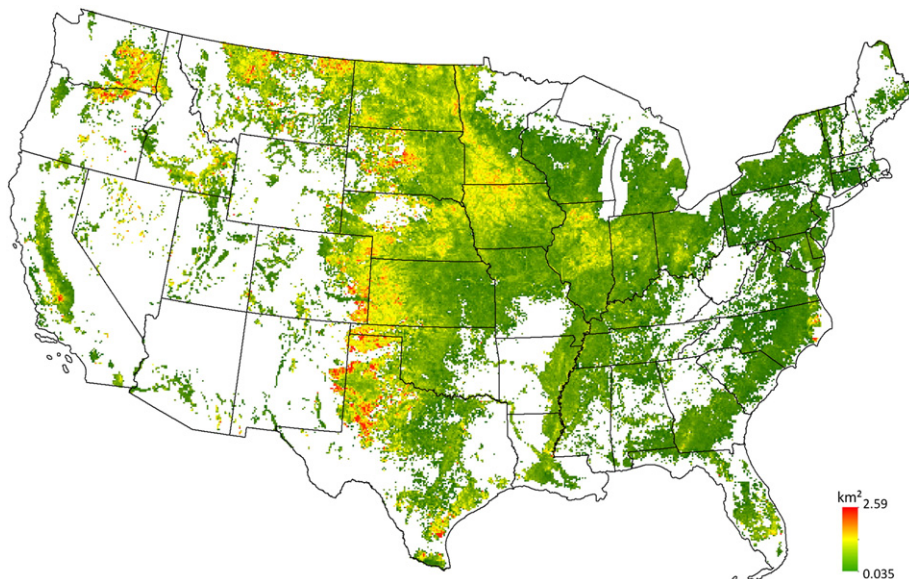


**Fig. 6.** CONUS extracted crop field size map for 2010. The mean field size in 7.5 km × 7.5 km gridcells is shown (colors) with state boundaries in black. The minimum non-zero (no agriculture) gridcell value is 0.035 km² and gridcell values greater than 2.59 km² (1 mile²) are set to 2.59 km² for visual clarity. Note that 1 km² = 100 ha = 247.1 acres.
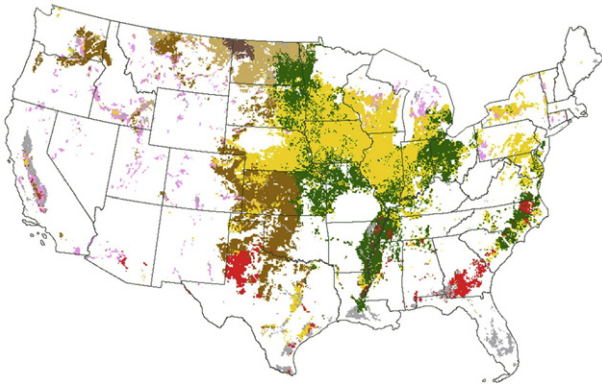
**Fig. 8.** Comparative CONUS 2010 CDL majority crop class. The majority CDL classes in 7.5 km × 7.5 km gridcells with ≥10% crop pixels are shown with the original CDL color legend for the major crops of corn, soybeans, alfalfa, winter wheat, spring wheat, durum wheat, and cotton, and the other crops are shown in gray. Gridcells with <10% crop pixels are shown in white and state boundaries are shown in black.

data (Yan & Roy, 2014). In addition, Google-Earth imagery (http://www.google.com/earth/) acquired close to the 2010 growing season that included high spatial resolution satellite and airborne images from a variety of commercial providers and US government agencies, and the 2010 CDL were inspected. This is because although field boundaries can be identified by visual inspection of appropriately displayed Landsat data, differentiation among croplands, managed grasslands and abandoned lands can be complex (Müller et al., 2015; Prishchepov, Radeloff, Dubinin, & Alcantara, 2012). In addition, adjacent fields planted with the same crop and agricultural management that are separated by a narrow boundary less than one Landsat pixel wide are hard to discriminate as separate fields (White & Roy, 2015; Yan & Roy, 2014).

Year 2010 Landsat 5 TM 30 m reflective wavelength bands and the 15 m panchromatic band panchromatic band (0.530–0.900 μm) were displayed in different displays. Image-processing software that allowed zooming, local contrast stretching, and rapid comparison of the Landsat

5 TM visible and panchromatic bands was used. An experienced geospatial analyst identified the field boundaries visually and digitized them into a standard polygon vector format with the 15 m pixel precision provided by the panchromatic band. A crop field was interpreted as one that had a prominent and contiguous boundary and the same crop type and agricultural management throughout its extent. The 2010 CDL was used to visually check that interpreted fields had the same majority crop type(s) across the field. An empirical "tractor rule" was used to resolve cases where the boundaries between adjacent fields were ambiguous to discern. In those cases, a boundary was defined if the analyst judged that a tractor could not easily cross the boundary, for example, if there was a tree line, hedge row, or fence, that were not observable on Landsat 5 data but visible in the Google-Earth imagery.

### 4.3. Accuracy measures

The independent reference field data for each of the 48 validation site locations were projected into the WELD Albers projection and rasterized at 30 m resolution for comparison with the extracted crop fields. The independent reference field data and the extracted field data were compared using conventional per-pixel and more recent object based accuracy measures. The rasterization process labeled a pixel as a crop field if the majority of the pixel was covered, and this combined with CONUS Landsat sub-pixel geolocation errors (Lee et al., 2004), will introduce some geolocation error between the data. Consequently, only extracted and independent reference fields overlapping each other by at least 5% were considered for the object-based accuracy assessment. All extracted fields that intersected the validation area boundaries were set to an unmapped status and excluded from the accuracy assessment.

Conventional per-pixel confusion matrix based accuracy measures were derived. A two-way confusion matrix populated with counts of the number of 30 m pixels classified as crop field or non-crop field classes in the extracted and the independent reference data were used to derive overall classification accuracy and field class user's and producer's accuracy statistics (Foody, 2002). In addition, the total number of reference field pixels, the total number of extracted field pixels,
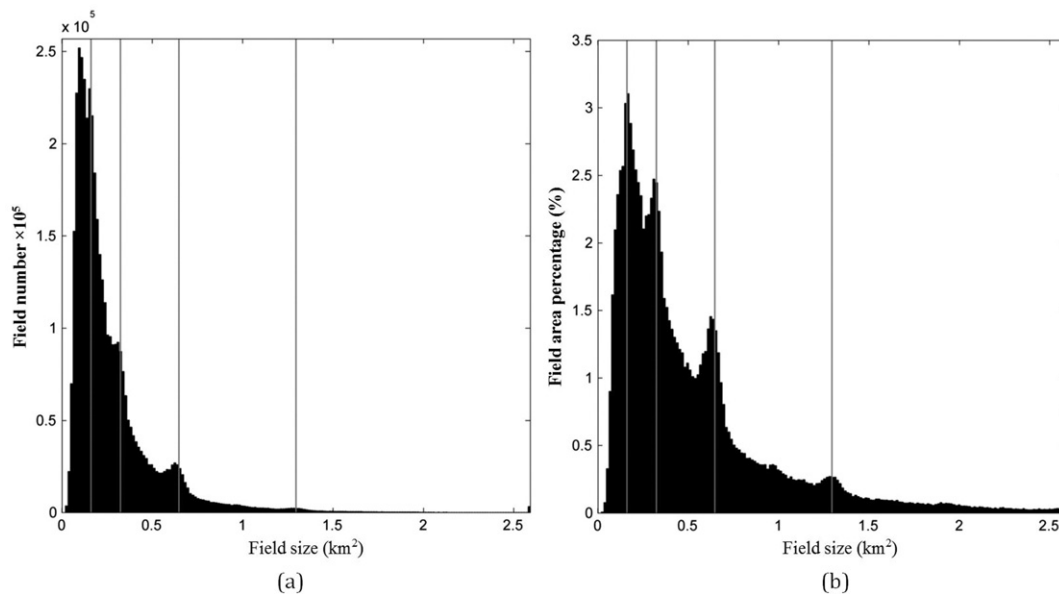


**Fig. 9.** CONUS field size histograms derived from all 4,182,777 extracted fields. (a) Histogram of number of fields, (b) Histogram of field area percentages (sum of all fields areas in each histogram bin expressed as a percentage of total extracted CONUS field area). The x-axis histogram bins are set as an area of 0.0144 km² i.e., equivalent to 16 Landsat 30 m pixels. The first histogram bin has no data plotted as fields with sizes less than 0.018 km² (20 pixels) were assumed to be too small to be extracted reliably. Fields larger than 1 × 1 mile (2.59 km²) were set to 2.59 km² for visual clarity. The vertical gray lines show the areas of hypothetical fields with side dimensions of 0.25 × 0.25 mile (0.162 km²), 0.25 × 0.5 mile (0.324 km²), 0.5 × 0.5 mile (0.646 km²), and 0.5 × 1 mile (1.295 km²).

(a)                                    (b)                                    (c)
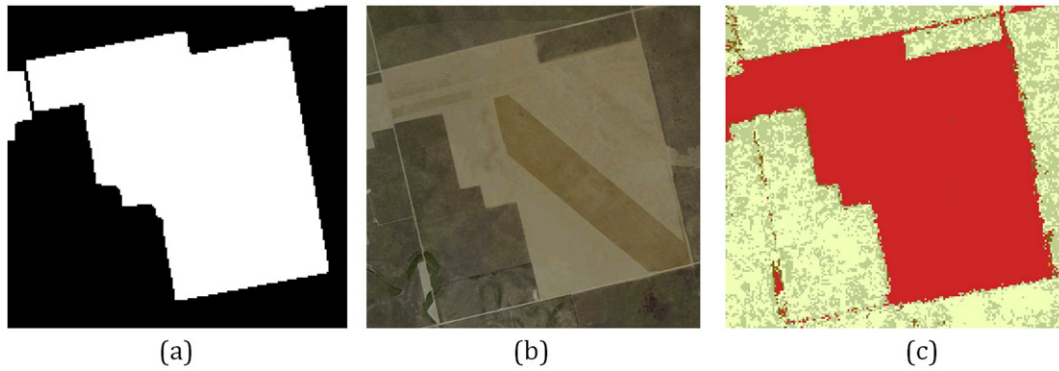
**Fig. 10.** The largest extracted CONUS field (12.955 km²) detected in Gaines, Texas (32.560920″ N, 102.312248″ W) (a) Extracted field, (b) Google-Earth imagery acquired August 18th 2010, (c) 2010 CDL data showing that the field is cotton (red) and the two primary surrounding land cover classes are grass/pasture (light lime) and shrubland (dark lime).

and the relative percentage difference in this total expressed as a percentage of the number of reference field pixels was derived.

The conventional per-pixel accuracy measures do not quantify the extraction accuracy of individual fields. Object extractions may be imperfect with errors that include the incorrect subdivision of larger objects into smaller ones (termed over-split or over-segmentation) and the consolidation of small adjacent objects into larger ones (termed under-split or under-segmentation). To capture the accuracy of the field extraction at the field, rather than pixel level, object extraction accuracy measures (Möller et al., 2013; Persello & Bruzzone, 2010; Yan & Roy, 2014) were used. The number of over- and under-split extracted fields (i.e. that were smaller or larger, respectively, than the reference fields) were defined. The number of one-to-one matched fields and the correctly matched percentage expressed as the percentage of one-to-one matched fields to the number of reference fields were derived. The total number and mean size (in pixels) of the reference and the extracted fields and the mean field size difference expressed as a percentage of the mean reference field size, were also derived.
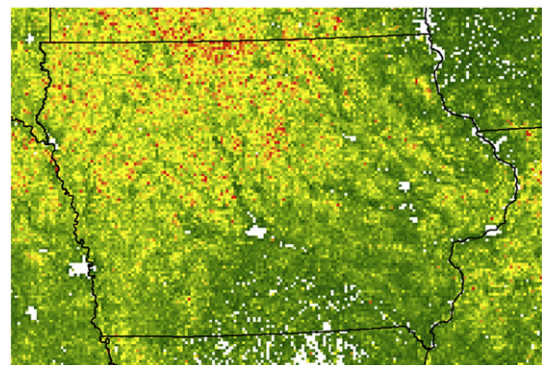


**Fig. 12.** Iowa extracted crop field size map for 2010. The mean field size in 3 km × 3 km gridcells is shown (colors) with state boundaries in black. Gridcells with no fields extracted (primarily urban areas and non-agricultural land uses) are shown in white. Note that 1 km² = 100 ha = 247.1 acres.



(a)                                                      (b)
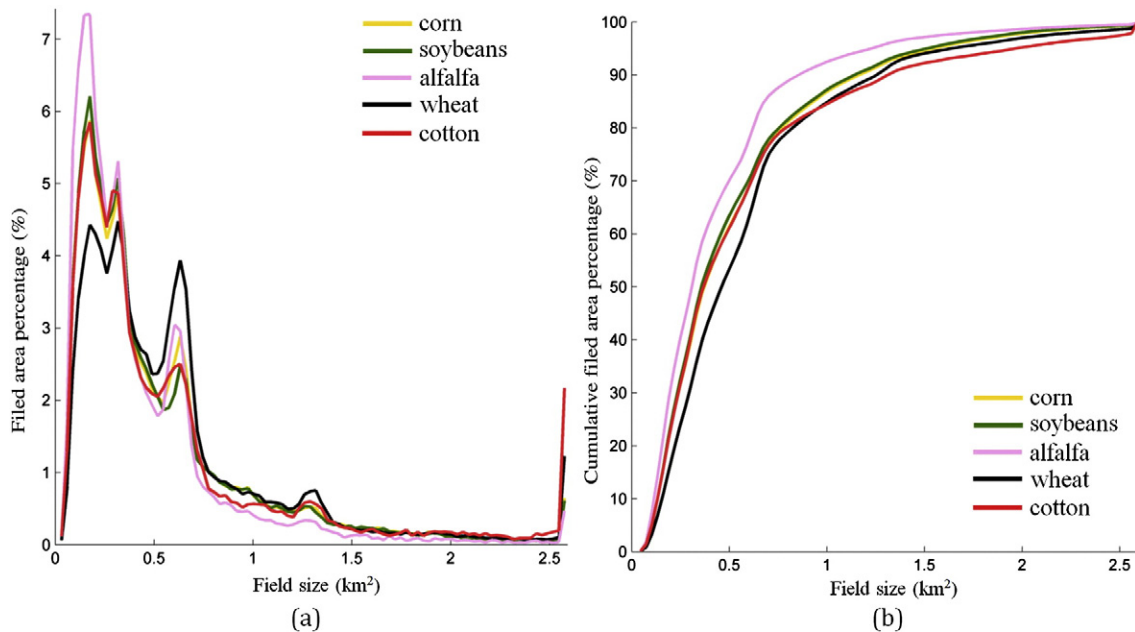
**Fig. 11.** CONUS field size histograms for the major crops: corn, soybeans, alfalfa, wheat (winter, spring and durum), and cotton. (a) Histogram of field area percentages of individual major crops (sum of all crop type fields areas in each histogram bin expressed as a percentage of total extracted CONUS crop type field area), (b) cumulative field area percentage histogram of individual major crops derived from (a). Only fields with more than 50% of its pixels labeled by the CDL 2010 crop type were considered providing a total of 1,107,224 (corn), 1,138,744 (soybeans), 238,654 (alfalfa), 557,431 (wheat) and 158,190 (cotton) CONUS extracted fields. For clarity, the x-axis histogram bins are set as an area of 0.0288 km² i.e., equivalent to 32 Landsat 30 m pixels.
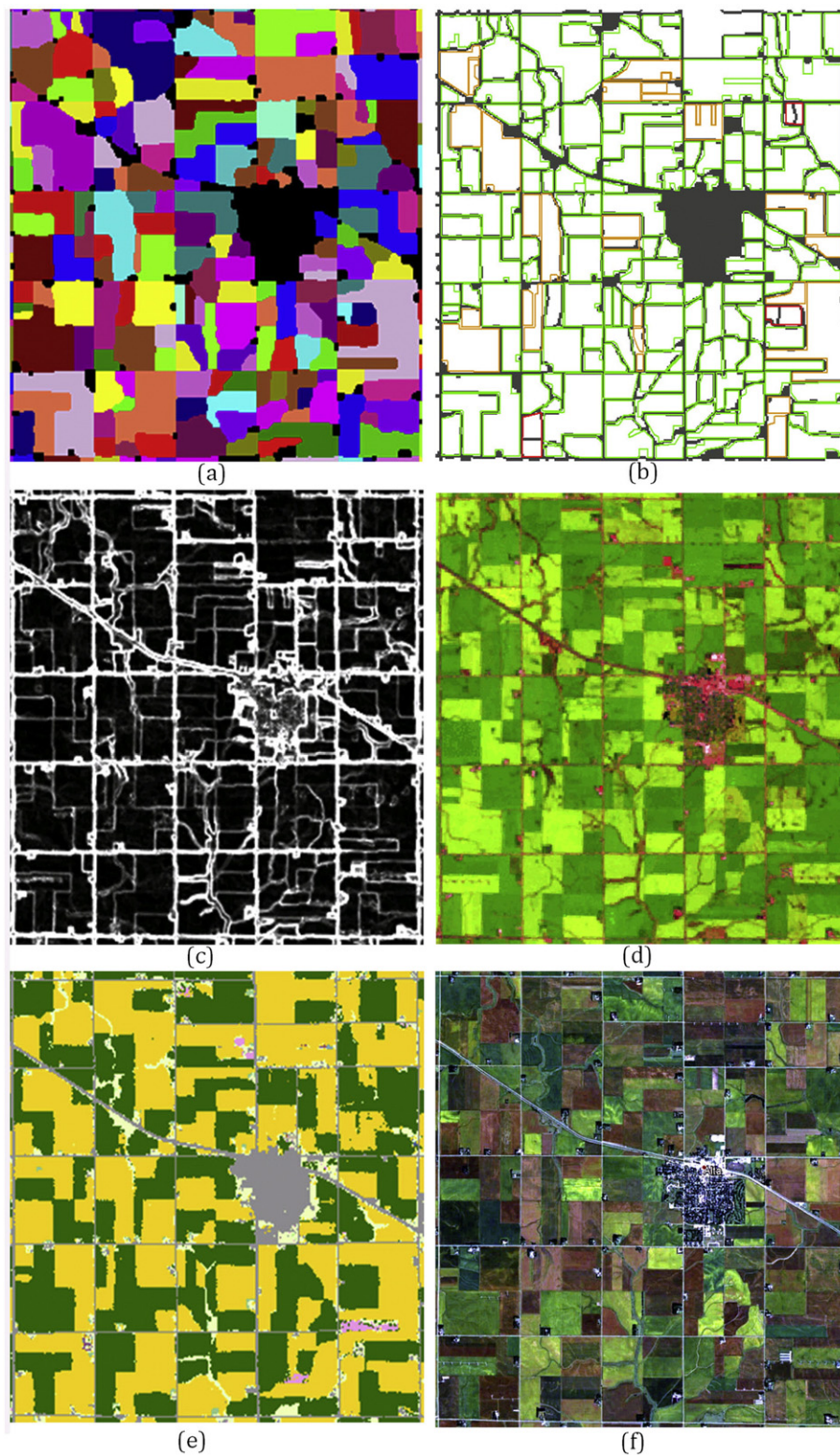
**Fig. 13.** Example validation site results for an 8.3 × 8.3 km region surrounding the small city of Alta, Iowa (population less than 2000). (a) Extracted crop fields colored randomly to illustrate they are separate objects (black indicates not a crop field), (b) independent reference field data (i.e., digitized field boundary polygon vectors) colored as green = one-to-one field match, red = extracted field over-split, orange = extracted field under-split, (c) Edge intensity map, (d) Landsat 5 false color image (bands 5, 4, 3) sensed in July 13th 2010, (e) USDA NASS CDL 2010 image showing major classes of corn, soybeans, alfalfa, grass/pasture, and developed/open space, (f) Google-Earth true color image sensed September 15th 2010.

## 5. CONUS results

Fig. 6 shows the extracted field sizes. Due to the spatial extent of the CONUS, composed of more than 11,000,000,000 30 m pixels, the mean field size in 7.5 km × 7.5 km gridcells is shown. To provide geographic and agricultural context, two comparative maps were derived from the 2010 CDL. Fig. 7 shows the percentage of each grid cell that was classified by the 2010 USDA NASS CDL as an agricultural crop class,

and Fig. 8 shows the gridcell majority crop class with respect to the CONUS major crops (corn, soybeans, alfalfa, winter wheat, spring wheat, durum wheat, and cotton). The field size extraction results appear highly plausible. In general, larger field sizes tend to occur where a greater proportion of the land is dedicated to agriculture (Fig. 7) and there are discernible patterns between field size and the majority crop type (Fig. 8).

Large field sizes (red tones, Fig. 6) occur in the Missouri and the Souris-Red-Rainy/Upper Mississippi river basins where about 50% of all U.S. cropland is located (U.S. Department of Agriculture, 2007) and these regions are quite evident in the CDL crop percentage map (Fig. 7). Large and intermediate field sizes (red and yellow tones, Fig. 6) are evident along the western sides of the Great Plains states from northern Texas to Montana, and also in the Columbia River basin in the Pacific Northwest, and occur where wheat is predominant (Fig. 8), sometimes termed the U.S. Wheat Belt (Hansen, Allen, Baumhardt, & Lyon, 2012; Norris, 1903). Regions of predominantly irrigated agriculture in eastern Colorado, western Kansas, western Oklahoma and the Texas panhandle and central California (Brown & Pervez, 2014) generally coincide with large field sizes. In particular, large field sizes are observed in the semi-arid Texas High Plains and central California where agricultural production relies extensively on irrigation. Large and intermediate field sizes occur around the Wheat belt and also in U.S. Corn Belt (Auch & Laingen, 2014; Chang, Hansen, Pittman, Carroll, & DiMiceli, 2007). Large fields in the Corn Belt are particularly evident in central South Dakota, southern Minnesota, and the northern parts of Iowa, Illinois, and Indiana. The large field sizes observed in North Carolina correspond to fertile historical wetland areas drained for agriculture (Poe, Piehler, Thompson, & Paerl, 2003; Richardson, 1983).

Fig. 9 shows the field size histograms of all the CONUS extracted fields. A total of 4,182,777 fields no less than 0.018 km$^2$ (20 30 m pixels) were extracted with mean and median field sizes of 0.193 km$^2$ and 0.278 km$^2$, respectively. The size of each field was calculated by counting the number of extracted field pixels and then multiplying by the area of a 30 × 30 m pixel (0.0009 km$^2$). The histograms show the number of fields (Fig. 9a) and the field area percentage defined as the sum of the fields areas in each histogram bin expressed as a percentage of the total extracted CONUS field area (Fig. 9b). The histograms are binned with an area equivalent to 16 Landsat pixels (0.014 km$^2$) in the same way as reported in (Yan & Roy, 2014). The four gray vertical lines show the sizes of hypothetical fields with 0.25 × 0.25 mile, 0.25 × 0.5 mile, 0.5 × 0.5 mile, and 0.5 × 1 mile side dimensions. The extracted CONUS fields frequently have areas similar to these dimensions. This is not surprising as much of the CONUS was surveyed using a grid survey system and land was allocated in equal subdivisions of a 1 × 1 mile grid (Meine, 2004; White, 1983). The four histogram peaks, most evident in Fig. 9(b), were 0.154 km$^2$, 0.311 km$^2$, 0.625 km$^2$ and 1.283 km$^2$ and are only slightly smaller than the hypothetical mile subdivision field areas (by 0.1%, 3.4%, 4.0% and 5.0% respectively) due to the quantization imposed by the 30 m Landsat pixel resolution and due to field extraction errors.

Of the more than 4.18 million extracted fields, only 3209 (0.08%) had areas greater than 1 × 1 mile (2.59 km$^2$). There were eight extracted fields with areas larger than 9 km$^2$. Four of them were in Texas, and the others were in Washington, Idaho, Colorado, and South Dakota. Of these, the two largest fields were found to be under-split, i.e., not separated into multiple fields, due to weak field boundaries between fields of the same crop type, and an extracted field in Colorado was found to not be a crop field but rather a grassland field due to a CDL classification error that mislabeled grassland as alfalfa. After discarding the three erroneous large fields, the largest remaining extracted CONUS field was a cotton field in Texas with an area of 12.955 km$^2$ (3200 acres) and a side length of approximately 4.25 km (Fig. 10). Examination of the available CDL data and Google-Earth imagery revealed that the field boundaries had not

changed and that the field was planted continuously with cotton from 2008 to 2014.

The CONUS is dominated by a few major crop types (Fig. 8, USDA 2012 Census). A total of 76.5% of the 4,182,777 extracted fields contained more than 50% CDL pixels classified as one of five major crop types, namely corn, soybean, alfalfa, wheat (winter, spring and durum), or cotton. Fig. 11 shows the CONUS field size histogram and cumulative field area percentage histogram derived independently for each of these major crops types. The frequent field size areas equivalent to the different mile subdivision areas remain evident. For all the CONUS, alfalfa fields are generally smaller than the other crop types, and the soybeans and corn have similar distributions, which is expected as these crops are often rotated between years (Plourde et al., 2013). Wheat fields are generally larger than the other crop types for sizes equivalent to between 0.5 × 0.5 mile (0.646 km$^2$) and 0.5 × 1 mile (1.295 km$^2$); and the largest fields tend to be cotton (as Fig. 10).

## 6. Iowa results

Fig. 12 shows a 3 km resolution field size map for Iowa selected because it has the greatest statewise harvested cropland area (USDA 2012 Census), a range of extracted field sizes (Fig. 6), and lies in the U.S. agricultural heart land (Fig. 7). Larger fields occur in north-west Iowa in a region of predominantly corn and soybean production, and urban areas and non-agricultural land uses are evident including Omaha on the western state border, Des Moines near the center of the state, and Waterloo, Ceder Rapids and Iowa City in the central eastern part of the state, and the Mississippi river and the city of Dubuque on the eastern state border. Examination of the 2010 CDL product indicates that the southern and eastern parts of Iowa are less agricultural and are predominantly covered by deciduous forest, grass, and pasture lands. The Iowa field size histogram is quite similar to the CONUS histogram but with a less pronounced field size peaks at sizes equivalent to 0.5 × 1 mile field sizes (1.295 km$^2$). A total of 308,917 fields were extracted in Iowa with a mean area of 0.330 km$^2$ and with areas ranging from 0.018 km$^2$ to 5.017 km$^2$.

Fig. 13 shows detailed full resolution field extraction results for a validation site in Iowa whose CONUS location is shown by the green dot in Fig. 5. The site encompasses the 7.5 km × 7.5 km gridcell in Iowa that had the median field size derived, as explained in Section 4.3, considering only state gridcells with more than 50% crop classified CDL pixels and containing at least 50 extracted fields. The illustrated field sizes and distributions are representative of the rest of Iowa, with variable field sizes constrained by 1 × 1 mile road intersections and certain irregular non-rectangular field boundaries associated often with irrigation features. The image is slightly larger than 5 × 5 miles (8.3 × 8.3 km) and is bigger than a 7.5 km × 7.5 km gridcell in order to avoid overly truncating fields along the image boundaries.

The results shown in Fig. 13 indicate generally good field extraction accuracy. The regular grid of metalled roads, and Highway 7 that runs from the North East to the South West, are apparent in the Landsat 5 (Fig. 13d) and Google-Earth (Fig. 13f) imagery and the extracted field boundaries do not cross them (Fig. 13a). The small city of Alta and the majority of the farm buildings (typically one to four farm houses and outbuildings, located at field edges or corners, per 1 × 1 mile section) are correctly detected with no extracted fields (Fig. 13a). The edge intensity map is illustrated (Fig. 13c) because as one of the fundamental intermediate results in the field extraction methodology (Fig. 1), it provides insights into how several of the field extraction errors occurred, and in addition, it captures field boundary information over the year of Landsat data that are not reflected in the single-date Landsat 5 and Google-Earth images. The Landsat 5 and Google-Earth images were acquired about two months apart, and the difference in the state of the fields is apparent due to harvesting and phenology. As noted in Yan and Roy (2014), the CDL product (Fig. 13e) does not capture field dimensions, which was not the purpose of the CDL product generation,

**Table 1**
Per-pixel accuracy metrics for the 48 validation sites (Fig. 5) referenced by the standard two letter U.S. state abbreviation where the number indicates if the site had the minimum (1), median (2), or maximum (3) field size considering the 7.5 km × 7.5 km gridcells in each state. Thus, the Iowa validation site (Fig. 13) results, that has the median Iowa gridcell field size, are reported as site IA2. The bottom table rows summarize the per-pixel accuracy results over all 48 sites.

| Site | Total number of independent reference field 30 m pixels (a) | Total number of extracted field 30 m pixels (b) | Percent field pixel count difference (b − a) / a × 100 | Field producer's accuracy | Field user's accuracy | Percent correctly classified as field or non-field pixels |
|---|---|---|---|---|---|---|
| IA 1 | 46,935 | 47,241 | 0.7% | 94.5% | 93.0% | 91.6% |
| IA 2 | 65,804 | 63,781 | −3.1% | 96.3% | 99.1% | 95.8% |
| IA 3 | 97,031 | 91,968 | −5.2% | 93.6% | 98.6% | 93.1% |
| SD 1 | 52,440 | 50,934 | −2.9% | 92.4% | 91.8% | 89.5% |
| SD 2 | 59,533 | 57,643 | −3.2% | 94.6% | 97.5% | 93.6% |
| SD 3 | 86,103 | 84,084 | −2.3% | 96.4% | 95.3% | 93.3% |
| ND 1 | 38,853 | 38,780 | −0.2% | 92.6% | 91.8% | 91.7% |
| ND 2 | 55,988 | 53,820 | −3.9% | 94.7% | 93.0% | 92.8% |
| ND 3 | 84,375 | 82,630 | −2.1% | 97.1% | 99.1% | 96.4% |
| TX 1 | 47,418 | 44,002 | −7.2% | 89.2% | 94.8% | 89.2% |
| TX 2 | 59,622 | 58,397 | −2.1% | 94.0% | 94.8% | 92.5% |
| TX 3 | 111,223 | 108,921 | −2.1% | 97.5% | 95.9% | 95.6% |
| NE 1 | 37,887 | 36,400 | −3.9% | 88.4% | 92.9% | 87.6% |
| NE 2 | 57,946 | 58,688 | 1.3% | 96.0% | 94.1% | 91.9% |
| NE 3 | 52,350 | 53,419 | 2.0% | 96.3% | 93.5% | 96.0% |
| KS 1 | 23,320 | 22,401 | −3.9% | 88.8% | 91.9% | 90.2% |
| KS 2 | 37,936 | 35,988 | −5.1% | 89.9% | 90.3% | 89.2% |
| KS 3 | 60,862 | 58,356 | −4.1% | 94.2% | 98.0% | 94.8% |
| OK 1 | 33,484 | 30,536 | −8.8% | 85.5% | 94.3% | 88.9% |
| OK 2 | 38,866 | 37,049 | −4.7% | 92.4% | 95.8% | 93.8% |
| OK 3 | 52,443 | 51,119 | −2.5% | 96.3% | 96.9% | 94.7% |
| MO 1 | 27,568 | 25,998 | −5.7% | 90.6% | 94.3% | 94.2% |
| MO 2 | 39,327 | 38,800 | −1.3% | 94.7% | 92.2% | 92.3% |
| MO 3 | 62,292 | 59,966 | −3.7% | 94.8% | 98.0% | 94.1% |
| MN 1 | 32,405 | 32,259 | −0.5% | 94.0% | 94.0% | 94.5% |
| MN 2 | 69,843 | 70,626 | 1.1% | 96.3% | 93.9% | 92.0% |
| MN 3 | 84,137 | 80,745 | −4.0% | 95.3% | 99.3% | 95.0% |
| IL 1 | 27,115 | 25,126 | −7.3% | 86.7% | 92.2% | 90.3% |
| IL 2 | 51,115 | 48,627 | −4.9% | 94.3% | 98.9% | 94.9% |
| IL 3 | 82,436 | 78,152 | −5.2% | 94.0% | 97.8% | 94.0% |
| IN 1 | 27,943 | 28,189 | 0.9% | 89.4% | 87.1% | 87.5% |
| IN 2 | 48,953 | 48,009 | −1.9% | 93.5% | 92.2% | 92.0% |
| IN 3 | 56,675 | 55,542 | −2.0% | 94.9% | 90.6% | 88.4% |
| OH 1 | 27,427 | 26,565 | −3.1% | 93.4% | 94.3% | 91.5% |
| OH 2 | 32,452 | 31,575 | −2.7% | 90.9% | 91.4% | 91.9% |
| OH 3 | 78,039 | 76,660 | −1.8% | 95.9% | 92.0% | 91.6% |
| AK 1 | 27,373 | 25,950 | −5.2% | 92.8% | 95.7% | 90.9% |
| AK 2 | 40,917 | 39,376 | −3.8% | 94.0% | 97.1% | 93.3% |
| AK 3 | 66,228 | 66,083 | −0.2% | 96.0% | 97.2% | 95.2% |
| MT 1 | 24,923 | 24,887 | −0.1% | 91.9% | 92.2% | 90.6% |
| MT 2 | 53,199 | 49,982 | −6.0% | 90.0% | 95.4% | 94.1% |
| MT 3 | 69,054 | 63,681 | −7.8% | 89.4% | 90.9% | 92.1% |
| WI 1 | 22,611 | 21,351 | −5.6% | 86.5% | 89.1% | 89.4% |
| WI 2 | 28,321 | 27,179 | −4.0% | 92.8% | 90.6% | 88.4% |
| WI 3 | 39,694 | 37,720 | −5.0% | 93.4% | 94.0% | 91.1% |
| CA 1 | 28,564 | 27,836 | −2.5% | 92.1% | 93.2% | 91.2% |
| CA 2 | 51,315 | 47,040 | −8.3% | 90.5% | 95.6% | 92.0% |
| CA 3 | 90,702 | 88,080 | −2.9% | 94.7% | 96.8% | 94.9% |
| *Summary statistics* | | | | | | |
| Min. | 22,611 | 21,351 | −8.8% | 85.5% | 87.1% | 87.5% |
| Max. | 111,223 | 108,921 | 2.0% | 97.5% | 99.3% | 96.4% |
| Mean. | 51,897 | 50,253 | −3.3% | 93.0% | 94.3% | 92.3% |
| Std. | 21,702 | 21,152 | 2.6% | 2.9% | 2.9% | 2.4% |
| Sum. | 2,491,047 | 2,412,161 | – | – | – | – |

and some CDL classification noise is apparent. The independent reference data (i.e., the digitized field boundary polygon vectors found by examination of the Landsat 5, Google-Earth and the 2010 CDL data) are shown (Fig. 13b) colored green to reflect correct correspondence, i.e. one to one matching, with the extracted fields; colored red where the extracted fields were too small, i.e., the extracted fields were incorrectly over-split into more than one field; and colored orange where the extracted fields were too big, i.e., were incorrectly under-split.

The Iowa validation results illustrated in Fig. 13b indicate generally good field extraction accuracy with 193 independent reference fields and 179 extracted fields, of which 159 were correctly matched providing an 82.4% matching percentage. There were a minority of three incorrectly over-split extracted fields (red) and fourteen incorrectly under-split extracted fields (orange). In general, in this and for the other validation sites, the over-split extracted fields occurred where there were ephemeral within field linear boundaries associated with flooding, seasonally inundated streams and ditches, and poorly drained depressions, that either occurred across a portion of the field or across all the field if it was small. The cause of the over-split field on the southern border is due to the presence of a subtle field boundary, seen with a weak edge intensity, that may or may not be real as is not unambiguously evident in the Landsat 5 or Google-Earth image.

**Table 2**
Field object accuracy metrics for the 48 validation sites (Fig. 5).

| Site | Number of independent reference fields (a) | Number of extracted fields (b) | Number of one-to-one matched fields (c) | Correctly matched percentage (c / a) × 100 | Number of over-split fields | Number of under-split fields | Mean independent reference field size (pixels)(d) | Mean extracted field size (pixels) (e) | Percentage mean field size difference (e − d / d) × 100 |
|---|---|---|---|---|---|---|---|---|---|
| IA 1 | 158 | 156 | 127 | 80.4% | 11 | 12 | 297.1 | 302.8 | 1.9% |
| IA 2 | 193 | 179 | 159 | 82.4% | 3 | 14 | 341.0 | 356.3 | 4.5% |
| IA 3 | 135 | 140 | 120 | 88.9% | 9 | 4 | 718.7 | 656.9 | −8.6% |
| SD 1 | 190 | 189 | 139 | 73.2% | 18 | 17 | 276.0 | 269.5 | −2.4% |
| SD 2 | 171 | 157 | 132 | 77.2% | 7 | 16 | 348.1 | 367.2 | 5.5% |
| SD 3 | 82 | 80 | 62 | 75.6% | 6 | 6 | 1050.0 | 1051.1 | 0.1% |
| ND 1 | 111 | 117 | 85 | 76.6% | 13 | 7 | 350.0 | 331.5 | −5.3% |
| ND 2 | 108 | 105 | 89 | 82.4% | 5 | 8 | 518.4 | 512.6 | −1.1% |
| ND 3 | 118 | 113 | 96 | 81.4% | 4 | 9 | 715.0 | 731.2 | 2.3% |
| TX 1 | 150 | 147 | 135 | 90.0% | 5 | 4 | 316.1 | 299.3 | −5.3% |
| TX 2 | 101 | 104 | 92 | 91.1% | 6 | 0 | 590.3 | 561.5 | −4.9% |
| TX 3 | 87 | 87 | 71 | 81.6% | 6 | 6 | 1278.4 | 1252.0 | −2.1% |
| NE 1 | 120 | 116 | 96 | 80.0% | 8 | 6 | 315.7 | 313.8 | −0.6% |
| NE 2 | 135 | 131 | 119 | 88.1% | 3 | 6 | 429.2 | 448.0 | 4.4% |
| NE 3 | 70 | 72 | 61 | 87.1% | 5 | 3 | 747.9 | 741.9 | −0.8% |
| KS 1 | 117 | 116 | 100 | 85.5% | 5 | 5 | 199.3 | 193.1 | −3.1% |
| KS 2 | 105 | 110 | 95 | 90.5% | 7 | 1 | 361.3 | 327.2 | −9.4% |
| KS 3 | 74 | 69 | 60 | 81.1% | 2 | 5 | 822.5 | 845.7 | 2.8% |
| OK 1 | 112 | 113 | 92 | 82.1% | 8 | 3 | 299.0 | 270.2 | −9.6% |
| OK 2 | 95 | 99 | 79 | 83.2% | 7 | 4 | 409.1 | 374.2 | −8.5% |
| OK 3 | 117 | 119 | 98 | 83.8% | 10 | 7 | 448.2 | 429.6 | −4.2% |
| MO 1 | 108 | 107 | 89 | 82.4% | 7 | 5 | 255.3 | 243.0 | −4.8% |
| MO 2 | 122 | 117 | 95 | 77.9% | 7 | 12 | 322.4 | 331.6 | 2.9% |
| MO 3 | 134 | 134 | 96 | 71.6% | 14 | 13 | 464.9 | 447.5 | −3.7% |
| MN 1 | 99 | 99 | 76 | 76.8% | 9 | 8 | 327.3 | 325.8 | −0.5% |
| MN 2 | 137 | 138 | 119 | 86.9% | 6 | 6 | 509.8 | 511.8 | 0.4% |
| MN 3 | 109 | 102 | 93 | 85.3% | 1 | 7 | 771.9 | 791.6 | 2.6% |
| IL 1 | 122 | 114 | 105 | 86.1% | 3 | 3 | 222.3 | 220.4 | −0.8% |
| IL 2 | 122 | 119 | 107 | 87.7% | 3 | 6 | 419.0 | 408.6 | −2.5% |
| IL 3 | 114 | 112 | 91 | 79.8% | 7 | 7 | 723.1 | 697.8 | −3.5% |
| IN 1 | 107 | 116 | 81 | 75.7% | 15 | 8 | 261.1 | 243.0 | −6.9% |
| IN 2 | 146 | 139 | 114 | 78.1% | 7 | 13 | 335.3 | 345.4 | 3.0% |
| IN 3 | 103 | 103 | 80 | 77.7% | 9 | 7 | 550.2 | 539.2 | −2.0% |
| OH 1 | 138 | 124 | 107 | 77.5% | 3 | 11 | 198.7 | 214.2 | 7.8% |
| OH 2 | 109 | 112 | 86 | 78.9% | 10 | 7 | 297.7 | 281.9 | −5.3% |
| OH 3 | 128 | 128 | 101 | 78.9% | 12 | 11 | 609.7 | 598.9 | −1.8% |
| AK 1 | 133 | 124 | 100 | 75.2% | 7 | 12 | 205.8 | 209.3 | 1.7% |
| AK 2 | 137 | 136 | 116 | 84.7% | 7 | 8 | 298.7 | 289.5 | −3.1% |
| AK 3 | 150 | 151 | 119 | 79.3% | 11 | 10 | 441.5 | 437.6 | −0.9% |
| MT 1 | 121 | 113 | 97 | 80.2% | 6 | 8 | 206.0 | 220.2 | 6.9% |
| MT 2 | 99 | 102 | 81 | 81.8% | 9 | 5 | 537.4 | 490.0 | −8.8% |
| MT 3 | 76 | 77 | 58 | 76.3% | 8 | 2 | 908.6 | 827.0 | −9.0% |
| WI 1 | 117 | 110 | 91 | 77.8% | 5 | 8 | 193.3 | 194.1 | 0.4% |
| WI 2 | 99 | 90 | 78 | 78.8% | 2 | 9 | 286.1 | 302.0 | 5.6% |
| WI 3 | 78 | 75 | 65 | 83.3% | 3 | 6 | 508.9 | 502.9 | −1.2% |
| CA 1 | 215 | 205 | 175 | 81.4% | 9 | 18 | 132.9 | 135.8 | 2.2% |
| CA 2 | 161 | 149 | 139 | 86.3% | 1 | 8 | 318.7 | 315.7 | −0.9% |
| CA 3 | 90 | 90 | 76 | 84.4% | 4 | 4 | 1007.8 | 978.7 | −2.9% |
| *Summary statistics* | | | | | | | | | |
| Min. | 70 | 69 | 58 | 71.6% | 1 | 0 | 132.9 | 135.8 | −9.6% |
| Max. | 215 | 205 | 175 | 91.1% | 18 | 18 | 1278.4 | 1252.0 | 7.8% |
| Mean. | 121 | 119 | 99 | 81.5% | 7 | 8 | 461.4 | 452.9 | −1.5% |
| Std. | 31 | 29 | 25 | 4.7% | 4 | 4 | 253.1 | 247.2 | 4.4% |
| Sum. | 5823 | 5705 | 4742 | – | 333 | 365 | – | – | – |

However, the other two over-split extracted fields, near the eastern border, occur where there is no evidence that they should be split into two fields when examining the Google-Earth image, although from inspection of the Landsat 5 image, the fields may be split where there is some form of drainage feature that is weakly apparent in the edge intensity image. Under-split extracted fields (orange) generally either occur due to weak field boundaries, for example, because the same crop type was planted in adjacent fields with narrow separations and/or because the boundary had vegetation with similar phenology as the crop, or where the fields contained smaller fields or other smaller features. In the illustrated results, these two types of under-split errors are quite apparent with several smaller quite complex under-split fields around the city of Alta and several large fields on the western and eastern borders that had the same CDL crop type and no clear internal edge

intensity boundary but were evident as separate fields in both the Google-Earth and Landsat 5 images. The empirical "tractor rule" was used to resolve cases where the boundaries between adjacent fields were ambiguous to discern. However, these examples illustrate the difficulty in unambiguously defining a field validation data set. Great efforts were expended on making a reliable independent reference data set but without the addition of high resolution satellite time series data, which were not freely available within the same year for such a large validation site sample, it would be hard to improve upon the validation data used.

## 7. Validation

Table 1 summarizes the conventional per-pixel accuracy statistics for each of the 48 validation sites and over all the sites. These results

indicate a high per-pixel crop field classification accuracy. The percent correct values range from 87.5% to 96.4% with a mean of 92.3% and a standard deviation of 2.4%, and the crop field producer's and user's accuracies are all greater than 85.5% and 87.1% respectively. These accuracies are high and comparable to reported 85% to 95% major crop 2010 CONUS CDL classification accuracies (Johnson, 2013). This is expected as the CDL was used to make a binary crop mask that was then used indirectly in the crop field extraction process (Fig. 1).

Considering the relative number of 30 m pixels in the extracted and in the independent reference fields provides insights into the area mapping accuracy of the field extraction. The percentage difference between the number of 30 m pixels in the extracted crop fields and in the independent reference fields vary over the 48 sites from −8.8% to 2.0% with a mean of −3.3% and a standard deviation of 2.6%. Thus, on average across the 48 sites, the areas of the extracted fields were slightly underestimated by about 3%. This is likely due to extraction errors including, for example, the morphological decomposition and postprocessing steps (Fig. 1), the quantization imposed by the 30 m Landsat pixel resolution, and because of the rasterization of the independent reference data. The extracted field size area underestimation was also evident in Fig. 9b where the four CONUS field size histogram peaks were smaller by 0.1%, 3.4%, 4.0% and 5.0% than the hypothetical mile subdivision field areas of 0.25 × 0.25 mile, 0.25 × 0.5 mile, 0.5 × 0.5 mile and 0.5 × 1 mile, respectively. Nevertheless, the results in Table 1 do not quantify the extraction accuracy of individual fields, and they do not capture field extraction over-splitting and under-splitting errors such as those illustrated in Fig. 13.

Table 2 summarizes the object extraction accuracy measures for each of the 48 validation sites and over all the sites. A total of 5823 independent reference data fields were selected from the 48 validation sites, with a mean of 121 fields and a range of 70 to 121 fields per site. Of the 5823 fields, a total of 4742 were correctly matched. Among the 48 validation sites, the correctly matched percentage varied from 71.6% to 91.1% with a mean of 81.5% and a standard deviation of 4.7%. These object based accuracy results are quite high. The sites with the lowest correctly matched percentage values were those with relatively more over- and under-split fields.

The mean size of the reference fields and the extracted fields are quite similar among the 48 sites. The percentage mean field size difference varied from −9.5% to 7.8% with a mean of −1.5% and a standard deviation of 4.4%. Considering only the correctly matched fields, the sizes of the extracted and independent reference fields were highly correlated with an ordinary least squares linear relationship of the form: *mean extracted field size* = 0.9711 × *mean reference field size* + 1.3880 (pixels) ($R^2 = 0.9730, n = 4742$). These results follow the same extracted field underestimate pattern evident in the per-pixel accuracy results.

The absolute number of over- and under-split fields was generally greater for sites with more independent reference fields. Among the 48 validation sites, seven sites (14.6%) had equal numbers of over- and under-split fields, 21 (43.8%) had more over-split fields, and 20 (41.7%) had more under-split fields. For the sites with equal numbers of over-split and under-split fields, the average percentage mean field size difference was −1.7%, i.e., close to the −1.5% average for all the sites. The average percentage mean field size difference for the sites that had more over-split fields was −4.9%, and for the sites that had more under-split fields was 2.2%. This is as expected because over-split and under-split fields will result in smaller and larger fields (compared with the independent reference fields), respectively.

There was no simple relationship between field size and the number of over- or under-split fields, and the causes of the over- and under-split fields were similar to those illustrated and explained with respect to the Fig. 13 results. Considering all the validation data without respect to which site they came from provided an overall accuracy assessment. There were a total of 2,491,047 and 2,412,161 references and extracted 30 m field pixels, respectively, i.e., the extracted fields underestimated

the reference field pixel count by 3.2%. The overall per-pixel crop field classification accuracy was 92.7% and the overall crop field producer's and user's accuracies were 93.7% and 94.9%. Comparing all the reference and extracted field objects, 81.4% were correctly matched and the extracted field sizes were on average underestimated by 1.2% relative to the reference field objects.

## 8. Conclusion

This paper has presented the comprehensive results of an automated computational methodology to extract agricultural crop fields from Landsat time series. For the first time, spatially explicit wall-to-wall Conterminous United States (CONUS) crop field size information is presented. The CONUS field size extraction results were highly plausible both geographically and with respect to the major U.S. harvested crop types. In general, larger field sizes tended to occur where a greater proportion of the land was dedicated to agriculture and there were discernible patterns between field size and major crop type. A total of 4,182,777 fields no less than 0.0018 km² were extracted with mean and median field sizes of 0.193 km² and 0.278 km² respectively. The largest field sizes predominantly occurred in the U.S. Wheat Belt and Corn Belt and in regions of irrigated agriculture. The CONUS field size histogram was skewed, which was observed in earlier field size studies considering smaller regions of the U.S. and Canada (Ferguson et al., 1986), and 50% of the extracted fields had sizes greater than or smaller than 0.361 km². The CONUS field size histogram had four distinct peaks that corresponded closely to sizes equivalent to fields with 0.25 × 0.25 mile, 0.25 × 0.5 mile, 0.5 × 0.5 mile, and 0.5 × 1 mile side dimensions. These dimensions reflect the historical land allocation of much of the United States. In this study, because only one year of Landsat data were used, "pie slice" circular sectors evident within circular pivot irrigation fields were extracted more often than full circular fields. Consequently, the dimensions of circular fields were not particularly apparent in the CONUS field size histogram.

The CONUS 2010 field extraction results were validated by comparison with Landsat 5 TM and Google-Earth images. Considering all the validation data at 48 sites, distributed across a gradient of field sizes in each of the top 16 harvested crop land area U.S. states, high field extraction accuracies were obtained. The overall per-pixel crop field classification accuracy was 92.7% and the overall crop field producer's and user's accuracies were 93.7% and 94.9%. Comparing all the reference and extracted field objects, 81.4% were correctly matched and the extracted field sizes were on average underestimated by 1.2% relative to the reference field objects.

Future work to consider the field size extraction results with respect to crop type is suggested. In this study, a CONUS examination found that 76.5% of the 4,182,777 extracted fields contained more than 50% CDL pixels classified as one of five major crop types, namely corn, soybean, alfalfa, wheat (winter, spring and durum), or cotton. Of these, alfalfa fields were generally smaller than the other crop types, and soybeans and corn fields had similar distributions which is expected as these crops are often rotated between years (Plourde et al., 2013). Wheat fields were generally larger than the other crop types for sizes equivalent to between 0.5 × 0.5 mile and 0.5 × 1 mile field sizes and the largest fields tended to be cotton.

Future work to characterize the field extraction results with respect to finer geographic units is recommended. For example, the field size histogram for certain states such as Iowa were found to have less pronounced field size peaks at sizes equivalent to 0.5 × 1 mile field sizes (1.295 km²) compared to the CONUS histogram. Different states may have different field size histograms reflecting quite different field size patterns due to a variety of factors, such as different historical land uses, soil fertility drainage, slope, and other geographic characteristics. Similarly, future work to compare the CONUS field size distribution with publically available farm size information is merited to see if there is a general relationship. This is because, among other reasons, large arable farms have been linked to mechanized farming practices

that may allow for more efficient use of resources and large field sizes but may lower crop diversity with detrimental environmental implications (Horrigan, Lawrence, & Walker, 2002; White & Roy, 2015).

The field extraction algorithm was refined based on the lessons learned from an earlier version of the algorithm (Yan & Roy, 2014). The major changes were to incorporate the CDL to reduce commission errors, especially to help differentiate between crops and grasslands. Also the algorithm was applied to one year of Landsat 5 TM and 7 ETM + data to reduce ambiguity due to crop rotations that can occur between years and to reduce the likelihood of physical field boundary changes that will increase when more years of data are used. Other refinements were made to make the algorithm more robust for CONUS-wide application; in particular, rather than use a simple edge intensity image derived from the year of Landsat data, edge saliency and linearity maps were derived following computer vision research to capture the degree to which intensity edges stand out locally relative to their neighbors and how linear the candidate edges were. The algorithm development was facilitated by the use of the geometrically corrected, preprocessed, and temporally composited Web Enabled Landsat Data (WELD). As noted in Yan and Roy (2014), the field extraction methodology is computationally intensive compared to supervised classification approaches that have been applied to CONUS WELD data (Egorov et al., 2015; Hansen et al., 2014), but it is sufficiently efficient and structured to be scalable to continental application. Future work to apply the algorithm to previous decades of Landsat data would help establish if field sizes have changed as has been reported at sample global locations (White & Roy, 2015). In addition, new moderate resolution satellite data, such as those provided by the Multi Spectral Instrument (MSI) on the planned Sentinel-2 satellite, which has Landsat-like bands but at 10 m & 20 m resolution (Drusch et al., 2012), and data provided by the Landsat 8 Operational Land Imager (OLI) that have better quantization and signal/noise characteristics than previous Landsat sensors (Roy et al., 2014), may provide improved field extraction capabilities especially in regions with smaller fields.

## Acknowledgments

## References

Anderson, M.C., Allen, R.G., Morse, A., & Kustas, W.P. (2012). Use of Landsat thermal imagery in monitoring evapotranspiration and managing water resources. *Remote Sensing of Environment, 122*, 50–65.

Auch, R.F., & Laingen, C. (2014). Having it both ways? Land use change in a U.S. Midwestern agricultural ecoregion. *The Professional Geographer, 67*, 84–97.

Bauer, M.E., Hixson, M.M., Davis, B.J., & Etheridge, J.B. (1978). Area estimation of crops by digital analysis of Landsat data. *Photogrammetric Engineering & Remote Sensing, 44*, 1033–1043.

Bleau, A., & Leon, L.J. (2000). Watershed-based segmentation and region merging. *Computer Vision and Image Understanding, 77*, 317–370.

Bogaert, J., Rousseau, R., Van Hecke, P., & Impens, I. (2000). Alternative area–perimeter ratios for measurement of 2D shape compactness of habitats. *Applied Mathematics and Computation, 111*, 71–85.

Boryan, C., Yang, Z., Mueller, R., & Craig, M. (2011). Monitoring US agriculture: The US department of agriculture, national agricultural statistics service, cropland data layer program. *Geocarto International, 26*, 341–358.

Boschetti, L., Roy, D.P., Justice, C.O., & Humber, M. (2015). MODIS–Landsat fusion for large area 30 m burned area mapping. *Remote Sensing of Environment, 161*, 27–42.

Bresenham, J.E. (1965). Algorithm for computer control of a digital plotter. *IBM Systems Journal, 4*(1), 25–30.

Bresson, X., Vandergheynst, P., & Thiran, J. (2006). A variational model for object segmentation using boundary information and shape prior driven by the Mumford–Shah functional. *International Journal of Computer Vision, 28*, 145–162.

Brown, J.F., & Pervez, M.S. (2014). Merging remote sensing data and national agricultural statistics to model change in irrigated agriculture. *Agricultural Systems, 127*, 28–40.

Caselles, V., Catte, F., Coll, T., & Dibos, F. (1993). A geometric model for active contours in image processing. *Numerische Mathematik, 66*, 1–31.

Chan, T., & Vese, L. (2001). Active contours without edges. *IEEE Transaction on Image Processing, 10*, 266–277.

Chang, J., Hansen, M.C., Pittman, K., Carroll, M., & DiMiceli, C. (2007). Corn and soybean mapping in the United States using MODIS time-series data sets. *Agronomy Journal, 99*, 1654–1664.

Chuvieco, E. (1999). Measuring changes in landscape pattern from satellite images: Short-term effects of fire on spatial diversity. *International Journal of Remote Sensing, 20*, 2331–2346.

Connor, D.J., Loomis, R.S., & Cassman, K.G. (2011). *Crop ecology, productivity and management in agricultural systems.* New York: Cambridge University Press.

Cremers, D., Rousson, M., & Deriche, R. (2007). A review of statistical approaches to level set segmentation: Integrating color, texture, motion and shape. *International Journal of Computer Vision, 72*, 195–215.

Drusch, M., Del Bello, U., Carlier, S., Colin, O., Fernandez, V., Gascon, F., ... Bargellini, P. (2012). Sentinel-2: ESA's optical high-resolution mission for GMES operational services. *Remote Sensing of Environment, 120*, 25–36.

Duveiller, G., & Defourny, P. (2010). A conceptual framework to define the spatial resolution requirements for agricultural monitoring using remote sensing. *Remote Sensing of Environment, 114*, 2637–2650.

Egorov, A.V., Hansen, M.C., Roy, D.P., Kommareddy, A., & Potapov, P.V. (2015). Image interpretation-guided supervised classification using nested segmentation. *Remote Sensing of Environment, 165*, 135–147.

Ferguson, M.C., Badhwar, G.D., Chhikara, R.S., & Pitts, D.E. (1986). Field size distributions for selected agricultural crops in the United States and Canada. *Remote Sensing of Environment, 19*, 25–45.

Field, D.J., Hayes, A., & Hess, R.F. (1993). Contour integration by the human visual system: Evidence for a local "association field". *Vision Research, 33*, 173–193.

Foody, G. (2002). Status of land cover classification accuracy assessment. *Remote Sensing of Environment, 80*, 185–201.

Fritz, S., See, L., McCallum, I., You, L., Bun, A., Moltchanova, E., ... Obersteiner, M. (2015). Mapping global cropland and field size. *Global Change Biology, 21*, 1980–1992.

Geiger, F., Bengtsson, J., Berendse, F., Weisser, W.W., Emmerson, M., Morales, M.B., ... Inchausti, P. (2010). Persistent negative effects of pesticides on biodiversity and biological control potential on European farmland. *Basic and Applied Ecology, 11*, 97–105.

Geisler, W.S., Perry, J.S., Super, B.J., & Gallogly, D.P. (2001). Edge co-occurrence in natural images predicts contour grouping performance. *Vision Research, 41*, 711–724.

Green, R.E., Cornell, S.J., Scharlemann, J.P.W., & Balmford, A. (2005). Farming and the fate of wild nature. *Science, 307*, 550–555.

Groom, M.J., & Schumaker, N. (1993). Evaluating landscape change: PATTERNS of worldwide deforestation and local fragmentation. In P.M. Kareiva, J.G. Kingsolver, & R.B. Huey (Eds.), *Biotic interactions and global change* (pp. 24–44). Sunderland: Sinauer Associates Inc.

Hansen, M.C., Egorov, A., Potapov, P.V., Stehman, S.V., Tyukavina, A., Turubanova, S.A., ... Bents, T. (2014). Monitoring conterminous United States (CONUS) land cover change with Web-Enabled Landsat Data (WELD). *Remote Sensing of Environment, 140*, 466–484.

Hansen, M.C., Egorov, A., Roy, D.P., Potapov, P., Ju, J., Turubanova, S., ... Loveland, T.R. (2011). Continuous fields of land cover for the conterminous United States using Landsat data: first results from the Web-Enabled Landsat Data (WELD) project. *Remote Sensing Letters, 2*, 279–288.

Hansen, N.C., Allen, B.L., Baumhardt, R.L., & Lyon, D.J. (2012). Research achievements and adoption of no-till, dryland cropping in the semi-arid U.S. Great plains. *Field Crops Research, 132*, 196–203.

Homer, C.G., Dewitz, J.A., Yang, L., Jin, S., Danielson, P., Xian, G., ... Megown, K. (2015). Completion of the 2011 national land cover database for the conterminous United States-representing a decade of land cover change information. *Photogrammetric Engineering and Remote Sensing, 81*, 345–354.

Horrigan, L., Lawrence, R., & Walker, P. (2002). How sustainable agriculture can address the environmental and human health harms of industrial agriculture. *Environmental Health Perspectives, 110*, 445–456.

Ji, C.Y. (1996). Delineating agricultural field boundaries from TM imagery using dyadic wavelet transforms. *ISPRS Journal of Photogrammetry and Remote Sensing, 51*, 268–283.

Johnson, D.M. (2013). A 2010 map estimate of annually tilled cropland within the conterminous United States. *Agricultural Systems, 114*, 95–105.

Johnson, D.M., & Mueller, R. (2010). The 2009 cropland data layer. *Photogrammetry Engineering & Remote Sensing, 76*, 1201–1205.

Ju, J., Roy, D.P., Vermote, E., Masek, J., & Kovalskyy, V. (2012). Continental-scale validation of MODIS-based and LEDAPS Landsat ETM + atmospheric correction methods. *Remote Sensing of Environment, 122*, 175–184.

Justice, C., Belward, A., Morisette, J., Lewis, P., Privette, J., & Baret, F. (2000). Developments in the validation of satellite products for the study of the land surface. *International Journal of Remote Sensing, 21*(17), 3383–3390.

Kovalskyy, V., & Roy, D.P. (2013). The global availability of Landsat 5 TM and landsat 7 ETM + land surface observations and implications for global 30 m Landsat data product generation. *Remote Sensing of Environment, 130*, 280–293.

Krebs, J.R., Wilson, J.D., Bradbury, R.B., & Siriwardena, G.M. (1999). The second silent spring? *Nature, 400*, 611–612.

Kuemmerle, T., Erb, K., Meyfroidt, P., Müller, D., Verburg, P.H., Estel, S., ... Reenberg, A. (2013). Challenges and opportunities in mapping land use intensity globally. *Current Opinion in Environmental Sustainability, 5*, 484–493.

Lee, D.S., Storey, J.C., Choate, M., & Hayes, R.W. (2004). Four years of Landsat-7 on-orbit geometric calibration and performance. *IEEE Transactions on Geoscience and Remote Sensing, 42*, 2786–2795.

Lee, D.T. (1982). Medial axis transformation of a planar shape. *IEEE Transactions on Pattern Analysis and Machine Intelligence, 4*, 363–369.

Li, W.W., Goodchild, M.F., & Church, R. (2013). An efficient measure of compactness for two-dimensional shapes and its application in regionalization problems. *International Journal of Geographical Information Science, 27*, 1227–1250.

Li, X., & Yeh, A.G.O. (2004). Analyzing spatial restructuring of land use patterns in a fast growing region using remote sensing and GIS. *Landscape and Urban Planning, 69*, 335–354.

Margosian, M.L., Garrett, K.A., & Hutchinson, J.S. (2009). Connectivity of the American agricultural landscape: assessing the national risk of crop pest and disease spread. *Bioscience, 59*, 141–151.

Marr, D. (1982). *Vision.* New York: Freeman and Company.

Martin, J. (2011). Perspective: Don't foul the water. *Nature, 474*, S17.

Masek, J.G., Vermote, E.F., Saleous, N.E., Wolfe, R., Hall, F.G., & Huemmrich, K.F. (2006). A Landsat surface reflectance dataset for North America, 1990–2000. *IEEE Transactions on Geoscience and Remote Sensing Letters, 3*, 68–72.

Meine, C. (2004). *Correction lines: essays on land, leopold, and conservation.* Island Press.

Möller, M., Birger, J., Gidudu, A., & Gläßer, C. (2013). A framework for the geometric accuracy assessment of classified objects. *International Journal of Remote Sensing, 34*, 8685–8698.

Morisette, J.T., Privette, J.L., & Justice, C.O. (2002). A framework for the validation of MODIS land products. *Remote Sensing of Environment, 83*, 77–96.

Moulin, S., Bondeau, A., & Delecolle, R. (1998). Combining agricultural crop models and satellite observations: from field to regional scales. *International Journal of Remote Sensing, 19*, 1021–1036.

Müller, H., Rufin, P., Griffiths, P., Barros Siqueira, A.J., & Hostert, P. (2015). Mining dense Landsat time series for separating cropland and pasture in a heterogeneous Brazilian savanna landscape. *Remote Sensing of Environment, 156*, 490–499.

Norris, F. (1903). *The pit.* New York: Doubleday, Page & Co.

O'Rourke, J. (1985). Finding minimal enclosing boxes. *International Journal of Computer and Information Sciences, 14*, 183–199.

Osher, S., & Sethian, J.A. (1988). Fronts propagating with curvature-dependent speed: Algorithms based on Hamilton–Jacobi formulations. *Journal of Computational Physics, 79*, 12–49.

Ozdogan, M. (2010). The spatial distribution of crop types from MODIS data: Temporal unmixing using independent component analysis. *Remote Sensing of Environment, 114*, 1190–1204.

Palmer, S.C.J., Kutser, T., & Hunter, P.D. (2015). Remote sensing of inland waters: Challenges, progress and future directions. *Remote Sensing of Environment, 157*, 1–8.

Papari, G., & Petkov, N. (2011). Edge and line oriented contour detection: State of the art. *Image and Vision Computing, 29*, 79–103.

Persello, C., & Bruzzone, L. (2010). A novel protocol for accuracy assessment in classification of very high resolution images. *IEEE Transactions on Geoscience and Remote Sensing, 48*, 1232–1244.

Pitts, D.E., & Badhwar, G. (1980). Field size, length, and width distributions based on LACIE ground truth data. *Remote Sensing of Environment, 10*, 201–213.

Plourde, J.D., Pijanowski, B.C., & Peki, B.K. (2013). Evidence for increased monoculture cropping in the central United States. *Agriculture, Ecosystems & Environment, 165*, 50–59.

Poe, A.C., Piehler, M.F., Thompson, S.P., & Paerl, H.W. (2003). Denitrification in a constructed wetland receiving agricultural runoff. *Wetlands, 23*, 817–826.

Prishchepov, A.V., Radeloff, V.C., Dubinin, M., & Alcantara, C. (2012). The effect of Landsat ETM/ETM+ image acquisition dates on the detection of agricultural land abandonment in Eastern Europe. *Remote Sensing of Environment, 126*, 195–209.

Ramachandra, C.A., & Mel, B.W. (2013). Computing local edge probability in natural scenes from a population of oriented simple cells. *Journal of Vision, 13*http://dx.doi.org/10.1167/13.14.19.

Richardson, C.J. (1983). Pocosins: Vanishing wastelands or valuable wetlands? *Bioscience, 33*, 626–633.

Roy, D.P., Ju, J., Kline, K., Scaramuzza, P.L., Kovalskyy, V., Hansen, M.C., ... Zhang, C. (2010). Web-enabled landsat data (WELD): Landsat ETM+ composited mosaics of the conterminous United States. *Remote Sensing of Environment, 114*, 35–49.

Roy, D.P., Wulder, M.A., Loveland, T.R., Woodcock, C.E., Allen, R.G., Anderson, M.C., ... Zhu, Z. (2014). Landsat-8: Science and product vision for terrestrial global change research. *Remote Sensing of Environment, 145*, 154–172.

Rudel, T.K., Schneider, L., Uriarte, M., Turner, B.L., DeFries, R., Lawrence, D., ... Grau, R. (2009). Agricultural intensification and changes in cultivated areas, 1970–2005. *Proceedings of the National Academy of Sciences of the United States of America, 106*, 20675–20680.

Rydberg, A., & Borgefors, G. (2001). Integrated method for boundary delineation of agricultural fields in multispectral satellite images. *IEEE Transactions on Geoscience and Remote Sensing, 39*, 2514–2519.

Serra, J. (1988). *Image analysis and mathematical morphology, volume 2: theoretical advances.* London: Academic Press.

Stehman, S.V. (2009). Sampling designs for accuracy assessment of land cover. *International Journal of Remote Sensing, 30*, 5243–5272.

Taylor, R. (1990). Interpretation of the correlation coefficient: A basic review. *Journal of Diagnostic Medical Sonography, 6*, 35–38.

Tsai, A., Yezzi, A., Jr., Wells, W., & Tempany, C. (2003). A shape-based approach to the segmentation of medical imagery using level sets. *IEEE Transactions on Medical Imaging, 22*, 137–154.

U.S. Department of Agriculture (2007). *Natural Resources Conservation Service.* National resources inventory.

U.S. Department of Agriculture (2008). U.S. Department of Agriculture Food, Conservation, and Energy Act. http://www.dm.usda.gov/foia/2008FCEA_Section1619.pdf

Wardlow, B.D., & Egbert, S.L. (2008). Large-area crop mapping using time-series MODIS 250 m NDVI data: An assessment for the U.S. Central Great Plains. *Remote Sensing of Environment, 112*, 1096–1116.

Whitcraft, A.K., Becker-Reshef, I., & Justice, C.O. (2015). A framework for defining spatially explicit earth observation requirements for a global agricultural monitoring initiative (GEOGLAM). *Remote Sensing, 7*, 1461–1481.

White, C.A. (1983). *A history of the rectangular survey system.* US Department of the Interior, Bureau of Land Management.

White, E., & Roy, D.P. (2015). A contemporary decennial examination of changing agricultural field sizes using Landsat time series data. *Geo: Geography and Environment*http://dx.doi.org/10.1002/geo2.4.

Yan, L., & Roy, D.P. (2014). Automated crop field extraction from multi-temporal Web Enabled Landsat Data. *Remote Sensing of Environment, 144*, 42–64.

Yan, L., & Roy, D.P. (2015). Improved time series land cover classification by missing-observation-adaptive nonlinear dimensionality reduction. *Remote Sensing of Environment, 158*, 478–491.

Yang, Y., Wilson, L.T., & Wang, J. (2014). Reconciling field size distributions of the US NASS (national agricultural statistics service) cropland data. *Computers and Electronics in Agriculture, 109*, 232–246.